














ARTICLE

The Rho regulator Myosin IXb enables nonlymphoid tissue seeding of protective CD8⁺ T cells

Federica Moalli¹ , Xenia Ficht¹ , Philipp Germann^{2,3,4} , Mykhailo Vladymyrov⁵ , Bettina Stolp¹ , Ingrid de Vries⁶, Ruth Lyck¹ , Jasmin Balmer⁷, Amleto Fiocchi⁸, Mario Kreutzfeldt⁹ , Doron Merkler⁹ , Matteo Iannacone¹⁰ , Akitaka Ariga⁵ , Michael H. Stoffel⁷ , James Sharpe^{2,3,4,11}, Martin Bähler¹², Michael Sixt⁶, Alba Diz-Muñoz¹³ , and Jens V. Stein¹ 

T cells are actively scanning pMHC-presenting cells in lymphoid organs and nonlymphoid tissues (NLTs) with divergent topologies and confinement. How the T cell actomyosin cytoskeleton facilitates this task in distinct environments is incompletely understood. Here, we show that lack of Myosin IXb (Myo9b), a negative regulator of the small GTPase Rho, led to increased Rho-GTP levels and cell surface stiffness in primary T cells. Nonetheless, intravital imaging revealed robust motility of Myo9b^{-/-} CD8⁺ T cells in lymphoid tissue and similar expansion and differentiation during immune responses. In contrast, accumulation of Myo9b^{-/-} CD8⁺ T cells in NLTs was strongly impaired. Specifically, Myo9b was required for T cell crossing of basement membranes, such as those which are present between dermis and epidermis. As consequence, Myo9b^{-/-} CD8⁺ T cells showed impaired control of skin infections. In sum, we show that Myo9b is critical for the CD8⁺ T cell adaptation from lymphoid to NLT surveillance and the establishment of protective tissue-resident T cell populations.

Introduction

Ag-specific T cells are exceedingly rare at the onset of an adaptive immune response (~1 clone per 10⁵ to 10⁶ T cells) (Tscharke et al., 2015). To expedite their encounter with cognate antigen, T cells have evolved to dynamically scan the surfaces of peptide-major histocompatibility complex (pMHC)-presenting cells. Studies using two-photon intravital microscopy (2PM) of mouse peripheral lymph nodes (PLNs) uncovered that parenchymal T cells move in an amoeboid manner on a three-dimensional network consisting of fibroblastic reticular cells (FRCs; Bajénoff et al., 2006), reaching high migratory speeds (10–15 μm/min). This scanning behavior allows them to efficiently interrogate dendritic cells (DCs) attached to the FRC scaffold (Katakai et al., 2013). Upon encounter of cognate pMHC and costimulatory molecules, T cells attach firmly to DCs for several hours and start to up-regulate activation markers (Huang et al., 2004; Sumen et al., 2004; Cahalan and Parker, 2006). After detachment from DCs, activated T cells proliferate before effector daughter cells exit via efferent lymphatic vessels or, in spleen, direct release into the blood circulation (Schwab and Cyster, 2007).

A key feature of recently activated effector CD8⁺ T cells is their switch from secondary lymphoid organ (SLO) recirculation to homing to nonlymphoid tissue (NLT), such as exocrine and endocrine glands, mucosal surfaces of the gut and reproductive tracts, skin epithelial barriers, or neuronal tissue (von Andrian and Mackay, 2000; Nolz, 2015). Compared with the widely spaced FRC scaffold of SLOs (Bajénoff et al., 2006; Novkovic et al., 2016), NLTs display highly divergent properties, including distinct adhesive or guidance molecules, topologies (e.g., isotropic vs. aligned collagen networks), rigidity (e.g., adipose vs. connective tissue), and confinement (e.g., prevention of cell extensions by tissue barriers; Charras and Sahai, 2014). Furthermore, T cell accumulation in NLTs requires transmigration in between or directly through endothelial cells with organ-specific adherens and tight junction protein composition (Furuse, 2009; Dejana and Orsenigo, 2013; Tietz and Engelhardt, 2015; Vestweber, 2015). Afterward, T cells have to breach the extracellular matrix (ECM)-rich basement membrane (BM) of endothelial cells, consisting of varying collagen and laminin networks cross-linked by

¹Theodor Kocher Institute, University of Bern, Bern, Switzerland; ²Centre for Genomic Regulation (CRG), The Barcelona Institute of Science and Technology, Barcelona, Spain; ³Universitat Pompeu Fabra (UPF), Barcelona, Spain; ⁴European Molecular Biology Laboratory, Barcelona, Spain; ⁵Albert Einstein Center for Fundamental Physics, Laboratory for High Energy Physics (LHEP), University of Bern, Bern, Switzerland; ⁶Institute for Science and Technology Austria, Klosterneuburg, Austria; ⁷Department of Clinical Research and Veterinary Public Health, University of Bern, Bern, Switzerland; ⁸Division of Immunology, Transplantation and Infectious Diseases, IRCCS San Raffaele Scientific Institute, Milan, Italy; ⁹Department of Pathology and Immunology, Division of Clinical Pathology, University and University Hospitals of Geneva, Geneva, Switzerland; ¹⁰Division of Immunology, Transplantation and Infectious Diseases and Experimental Imaging Center, IRCCS San Raffaele Scientific Institute and Vita-Salute San Raffaele University, Milan, Italy; ¹¹Institució Catalana de Recerca i Estudis Avançats (ICREA), Barcelona, Spain; ¹²Institut für Molekulare Zellbiologie, Westfälische Wilhelms-Universität Münster, Münster, Germany; ¹³Cell Biology and Biophysics Unit, European Molecular Biology Laboratory, Heidelberg, Germany.

Correspondence to Jens V. Stein: jstein@tki.unibe.ch.

© 2018 Moalli et al. This article is distributed under the terms of an Attribution–Noncommercial–Share Alike–No Mirror Sites license for the first six months after the publication date (see <http://www.rupress.org/terms/>). After six months it is available under a Creative Commons License (Attribution–Noncommercial–Share Alike 4.0 International license, as described at <https://creativecommons.org/licenses/by-nc-sa/4.0/>).

nidogens, perlecan, and other proteins (Kalluri, 2003; Pfeiffer et al., 2008; Rowe and Weiss, 2008; Nourshargh et al., 2010; Yousif et al., 2013). Finally, in barrier organs (e.g., skin and gut) or secretory glands (e.g., salivary glands), effector CD8⁺ T cells migrate from connective tissue into epithelial layers, which requires crossing of the epithelial BM (Breitkreutz et al., 2009; Cauley and Lefrançois, 2013; Smith et al., 2015; Thom et al., 2015). In skin, this process is facilitated by CXCR3 ligands synthesized by keratinocytes (Mackay et al., 2013). After clearance of an infection, CD62L⁺CCR7⁺ central memory T cells (T_{CM}) scan lymphoid tissue for fast recall responses, whereas CX3CR1^{int}CD62L⁺CCR7⁺ peripheral memory T cells and CX3CR1^{high}CD62L⁺CCR7⁺ effector memory T cells patrol NLTs and blood, respectively (Sallusto et al., 2004; Gerlach et al., 2016). Recent studies have shown that many NLTs, including mucosal surfaces, salivary glands, and epidermis, are continuously surveilled by CD69⁺CD103⁺ tissue-resident memory CD8⁺ T cells (T_{RM}) that persist after pathogen clearance for prolonged periods of time. In these exposed organs, T_{RM} rapidly induce recall responses for tissue-wide protection upon reinfection (Ariotti et al., 2014; Iijima and Iwasaki, 2014; Schenkel et al., 2014; Stary et al., 2015). Thus, all stages of adaptive immune responses require efficient CD8⁺ T cell motility, from the rapid selection of appropriate clones in lymphoid tissue to the accumulation of effector T cells (T_{EFF}) at sites of infection and the continuous surveillance of SLOs and NLT by memory T cell populations.

Migrating leukocytes are characterized by a polarized shape with F-actin-rich protrusions at the leading edge and actomyosin contractions at the uropod (Krummel and Macara, 2006; Friedl and Weigelin, 2008; Paluch et al., 2016). Polarization is stabilized by the spatially segregated activation of guanine exchange factors (GEFs) and GTPase-activating proteins (GAPs). These enzymes control small GTPases of the Rho/Ras family by switching them from their inactive GDP-bound state to their active GTP-bound state and back (Tybulewicz and Henderson, 2009; Rougerie and Delon, 2012; Niggli, 2014). Active Rac-GTP and Cdc42-GTP at the leading edge of migrating cells enable continuous WAVE/Scar-Arp2/3-mediated F-actin polymerization required for pseudopod protrusion (Renkawitz et al., 2009; Faroudi et al., 2010; Ridley, 2011; Fritz-Laylin et al., 2017). At the trailing edge, Rho-GTP signals through a Rho-associated protein kinase (ROCK)-Myosin light chain (MLC)-nonmuscle Myosin II pathway to promote uropod contractions for detachment from adhesive surfaces and for nuclear propulsion (Morin et al., 2008; Lämmermann and Sixt, 2009; Jacobelli et al., 2010). In addition, F-actin treadmilling and actomyosin contractility of the cell cortex determine the general biophysical properties of cells, such as cell surface elasticity, cell cortex tension, and in-plane membrane tension (Renkawitz and Sixt, 2010; Gauthier et al., 2012; Diz-Muñoz et al., 2013; Krummel et al., 2014; Bergert et al., 2015). Yet, although these properties have been assigned to decisive roles during developmental processes and cancer metastasis, there is scarce information on how cell surface mechanics are regulated in T cells and how they contribute to organ-specific adaptive immune responses.

Myosin IXb (Myo9b) is an F-actin-based cytoskeletal motor protein with a RhoGAP activity as intramolecular cargo. It

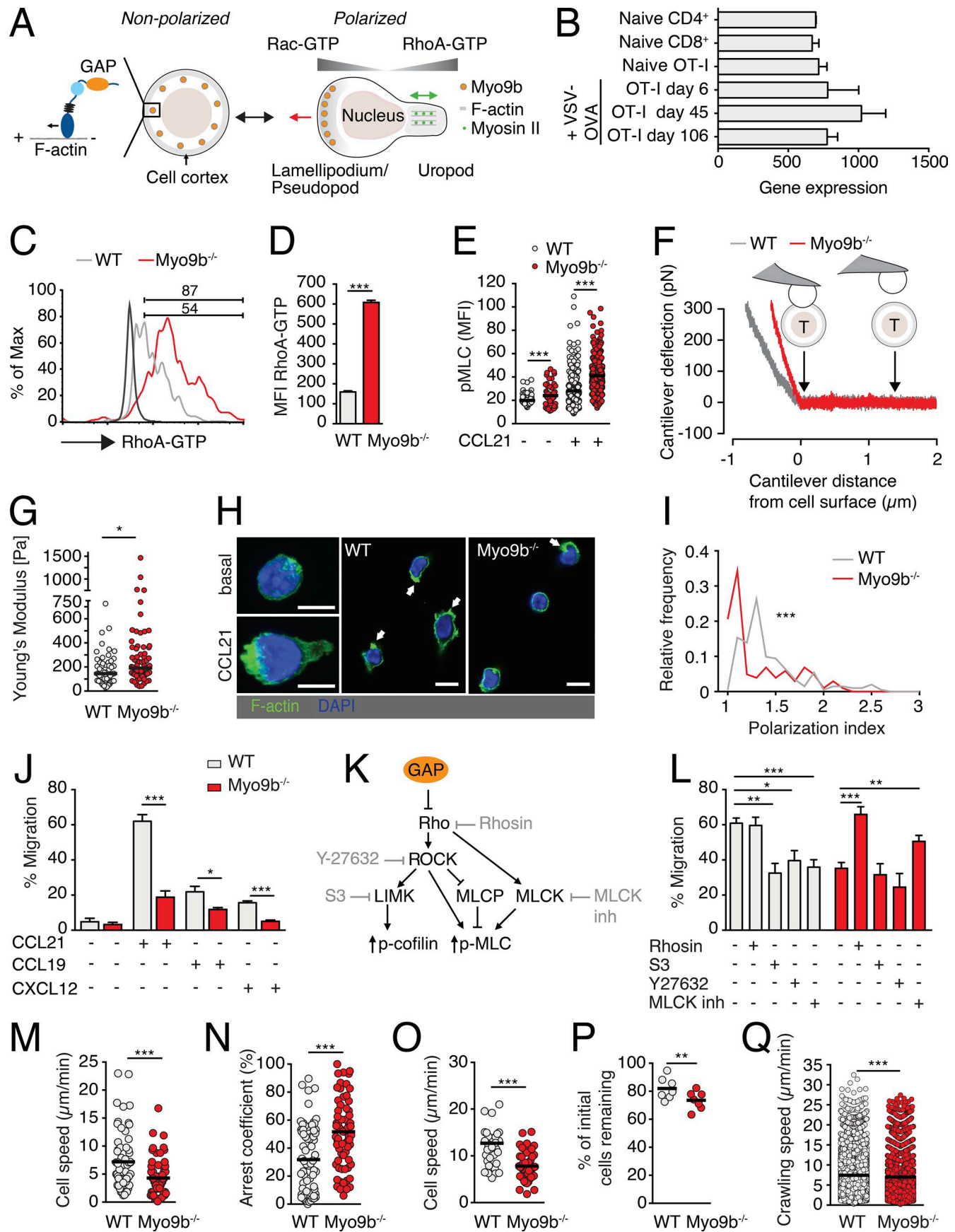
accumulates at the leading edge of polarized macrophages and DCs (van den Boom et al., 2007; Hanley et al., 2010; Xu et al., 2014). In these cell types, Myo9b deficiency leads to increased steady-state Rho-GTP levels and a contracted cell phenotype (Hanley et al., 2010; Xu et al., 2014). A role for Myo9b in naive and effector/memory CD8⁺ T cells has not yet been explored. Here, we show that CD8⁺ T cells lacking Myo9b have high steady-state Rho-GTP levels and a significantly increased resistance to elastic deformation that correlated with reduced chemotaxis in vitro. Nonetheless, Myo9b^{-/-} CD8⁺ T cells showed robust homing to SLOs and comparable clonal expansion and effector differentiation as their WT counterparts during DC- or virus-triggered immune responses. In contrast, Myo9b^{-/-} effector/memory CD8⁺ T cells failed to efficiently seed NLTs. 2PM intravital imaging and functional assays revealed that Myo9b is required for cells to cross dense ECM barriers such as the BM between dermis and epidermis, but less so for motility within 3D confined environments. Collectively, our data suggest that Myo9b-dependent regulation of Rho activity enables CD8⁺ T cells to establish protective effector and memory T cell populations in NLTs.

Results

Myo9b regulates Rho-GTP levels and surface stiffness in primary T cells

Myo9b is a motorized RhoGAP that negatively controls Rho activity in myeloid cells (Fig. 1 A; van den Boom et al., 2007; Hanley et al., 2010). Microarray data from the ImmGen resource (Heng et al., 2008) showed that Myo9b is also constitutively expressed in naive and effector/memory T cells (Fig. 1 B), with only a transient decrease in expression levels early after viral infection. As this suggested a function for this protein in adaptive immune responses, we examined how lack of Myo9b affects T cell properties. Primary Myo9b^{-/-} T cells showed a bona fide CD62L^{high}CD44^{low} naive phenotype and expressed CCR7 and LFA-1 at WT T cell levels (Fig. S1). In contrast, Myo9b^{-/-} T cells displayed significantly increased steady-state Rho-GTP levels (Fig. 1, C and D) and augmented levels of the Rho downstream effector pMLC, both with and without CCL21 stimulation (Fig. 1 E).

Because Myo9b and small GTPases including Rho act at the cell cortex, and cell cortex contractility affects surface elasticity (Krieg et al., 2008; Cai et al., 2010), we used atomic force microscopy (AFM) to examine the surface mechanics of ConA-stimulated WT and Myo9b^{-/-} CD8⁺ T cells (Fig. 1 F). In these assays, the deflection of the AFM cantilever correlates with the resistance to deformation for up to 200 nm below the cell surface. This assay therefore measures the mechanical properties of the cell surface including the cortical F-actin network. The Young's modulus of elasticity, which is a measure of an object's resistance to being deformed elastically when a force is applied to it, was tightly regulated around 145 ± 18 Pa (mean ± SEM) in WT T cells. In contrast, Myo9b^{-/-} CD8⁺ T cells showed a significantly increased Young's modulus (191 ± 27 Pa) as compared with WT T cells, with some cells showing a Young's modulus of around 1 kPa (Fig. 1 G). Collectively, Myo9b activity regulates RhoA-GTP levels in primary T cells and the mechanical properties of the cell surface.



Myo9b is required for in vitro polarization and migration of T cells

We examined the impact of Myo9b deficiency on T cell behavior in vitro. After stimulation with CCL21, Myo9b^{-/-} T cells displayed a more rounded phenotype with fewer F-actin ruffles as compared with WT T cells (Fig. 1 H), resulting in impaired polarization (Fig. 1 I). In line with this finding, Myo9b^{-/-} T cells migrated significantly less to the homeostatic chemokines CXCL12, CCL19, and CCL21 in Transwell assays (Fig. 1 J). We obtained similar results when we analyzed migration of Myo9b^{-/-} B cells toward homeostatic chemokines, indicating that Myo9b facilitates chemotactic responses in all lymphocytes (unpublished data). To assess whether increased Rho-GTP levels were directly responsible for the observed migration defect, we treated T cells with pharmacological inhibitors of signaling pathways downstream of active RhoA (Fig. 1 K). Direct blocking of Rho-GTP formation by 1 μ M Rhosin (Shang et al., 2012) or inhibition of myosin light chain kinase (MLCK), but not ROCK or LIM domain kinase 1 (LIMK), rescued the chemotactic response of Myo9b^{-/-} T cells to WT T cell levels (Fig. 1 L). We next asked whether absence of Myo9b affected T cell blast motility in geometrically more complex 3D collagen matrices, a reductionist model for interstitial migration. Myo9b^{-/-} T cell speeds were reduced compared with WT T cells (7.2 ± 5.0 μ m/min for WT and 4.3 ± 3.1 μ m/min for Myo9b^{-/-} T cells; mean \pm SD), whereas arrest coefficients (i.e., the percentage of track segments slower than 5 μ m/min) were increased (Fig. 1, M and N). We obtained similar results when we compared WT and Myo9b^{-/-} T cell blast migration under agarose, a model for 2D confined environments (Fig. 1 O). A comparable reduction (30–40%) of Myo9b^{-/-} T cells speeds was observed on laminin 411, 511, or collagen IV-coated slides (unpublished data). In contrast, lack of Myo9b had only a minor effect on shear flow resistance, as most WT and Myo9b^{-/-} T cells remained attached to ICAM-1 + CCL21-coated plates under flow (Fig. 1 P) despite reduced crawling speeds for Myo9b^{-/-} T cells (Fig. 1 Q). In sum, our analysis suggests that Myo9b is required for optimal in vitro motility, whereas integrin-mediated adhesion under flow was largely unaffected.

In vivo T cell homing and interstitial motility in SLOs are largely preserved in Myo9b^{-/-} T cells

To address the physiological role of Myo9b, we investigated the steady-state lymphocyte compartment of Myo9b^{-/-} mice. Absence of Myo9b resulted in decreased T cell numbers in the thymus, whereas percentages of CD4/CD8 single and double positive cells and early double negative thymocyte differentiation marker expression were comparable to WT counterparts (Fig. S2, A and B). Similarly, analysis of bone marrow suspensions revealed normal B cell development in the absence of Myo9b (unpublished data). The overall compartmentalized architecture of Myo9b^{-/-} lymph nodes (LNs) with distinct T and B cell zones was largely preserved, although the spacing of the ECM network produced by FRCs was more compact, suggesting decreased cellularity. In agreement with this, T cell numbers in SLOs were reduced by \sim 50% in Myo9b^{-/-} as compared with WT mice (Fig. S2, C and D). As isolated Myo9b^{-/-} lymphocytes did not show increased apoptosis compared with WT T cells (unpublished data), we explored alternative mechanisms leading to decreased SLO cellularity. To examine nonhematopoietic cells as cause for reduced thymic and peripheral T cell numbers, we created bone marrow chimera by transferring CD45.1⁺CD45.2⁺ and CD45.2⁺ WT or Myo9b^{-/-} bone marrow into lethally irradiated CD45.1⁺ C57BL/6 mice. After 8 wk, bone marrow, thymus, spleen, mesenteric LNs (MLNs), and PLNs were analyzed by flow cytometry. Whereas normalized WT-WT reconstitution ratios were comparable, Myo9b^{-/-} bone marrow gave rise to significantly fewer lymphocytes as compared with WT bone marrow (Fig. S2, E and F). Collectively, lack of Myo9b caused a T cell-intrinsic lymphopenia in thymus and SLOs that became aggravated under competitive conditions.

Based on in vitro data and the phenotype of Myo9b^{-/-} mice, we hypothesized that Myo9b deficiency translates into defective trafficking patterns of naive T cells in vivo. However, adoptive transfer experiments into WT hosts uncovered only a minor reduction of Myo9b^{-/-} T cells homing to SLOs at 2 h after transfer (Fig. 2 A). To identify the microanatomical location of transferred T cells, we performed ultrashort homing assays, followed by three-dimensional LN reconstructions (Soriano et al., 2011). This sensitive assay exposed a minor reduction of Myo9b^{-/-} T cell

Figure 1. In vitro characterization of primary Myo9b^{-/-} T cells. (A) Outline of nonpolarized versus polarized T cell with small GTPase activity and Myo9b distribution, including a scheme of its RhoGAP "cargo." The red arrow of the polarized cell indicates direction of movement, whereas the green arrow indicates uropod contractility. (B) Myo9b gene expression of naive and vesicular stomatitis virus (VSV)-OVA-activated effector and memory T cells isolated from spleen. Data are from ImmGen database. (C) Flow cytometry plot of RhoA-GTP levels in resting WT (gray line) and Myo9b^{-/-} T cells (red line). The black line depicts background, numbers indicate percentage of positive cells. (D) MFI of RhoA-GTP in WT and Myo9b^{-/-} T cells. Shown is mean \pm SEM. Pooled from three mice per genotype in one experiment. (E) MFI of pMLC in WT and Myo9b^{-/-} T cells. Pooled from five mice in two independent experiments. (F) Experimental layout of AFM-based surface elasticity measurement. The gray and red lines are representative measurements of cantilever deflection after bead contact to WT or Myo9b^{-/-} CD8⁺ T cells. (G) Young's modulus of elasticity of WT and Myo9b^{-/-} CD8⁺ T cells. Pooled from two independent experiments. (H) Fluorescent images of WT and Myo9b^{-/-} T cells before and after CCL21 stimulation. Arrows indicate F-actin-containing membrane protrusions. Bars, 5 μ m. (I) Polarization index of WT (gray line) and Myo9b^{-/-} (red line) T cells. Pooled from two independent experiments with a total of 202 WT and 142 Myo9b^{-/-} T cells. (J) Transwell migration of WT and Myo9b^{-/-} T cells toward CCL21, CCL19, and CXCL12. Shown is mean \pm SEM. Pooled from two to five independent experiments. (K) Scheme of Rho signaling pathways and selected inhibitors. (L) Transwell migration of WT and Myo9b^{-/-} T cells to CCL21 in presence of indicated inhibitors. Shown is mean \pm SEM. Pooled from four independent experiments. (M) Migration speeds of WT and Myo9b^{-/-} T cell blasts in a 3D collagen matrix. (N) Arrest coefficient of WT and Myo9b^{-/-} T cell blasts in a 3D collagen matrix. Data in G and H are pooled from four mice per genotype in two independent experiments. (O) Under agarose speeds of WT and Myo9b^{-/-} T cell blasts from one experiment. (P) Sustained shear-resistant adhesion of naive WT and Myo9b^{-/-} T cells in flow chamber. Shown are percentages of T cells that resisted detachment from ICAM-1 + CCL21 after 10 min of high shear. Pooled from two independent experiments. (Q) Crawling speeds of WT and Myo9b^{-/-} T cells on ICAM-1 + CCL21 under physiological shear. Pooled from four independent experiments. Statistical analysis: unpaired Student's *t* test (D, E, J, M, N, and O); Mann-Whitney test (G, I, and Q); paired *t* test (P); ANOVA with Sidak's multiple comparison test against "no inhibitor" (L). *, *P* < 0.05; **, *P* < 0.01; ***, *P* < 0.001. Horizontal bars depict mean.

numbers within the parenchyme as compared with WT T cells, while these cells were accumulating in the perivascular space (Fig. 2, B and C). Next, we performed intravital 2PM imaging of PLNs to assess dynamic motility parameters of Myo9b^{-/-} T cells in situ. In contrast to our in vitro migration data, 2PM tracking of T cells in popliteal LNs revealed a remarkably robust interstitial motility of Myo9b^{-/-} T cells (Fig. 2 D and Video 1), with only minor alterations as compared with WT T cells. Thus, occasional Myo9b^{-/-} T cells showed signs of sudden contraction or U-turns between periods of normal motility (Video 2). A detailed analysis of intravital image sequences with high temporal resolution further revealed that Myo9b^{-/-} T cells were on average more rounded, a phenotype that correlated with a minor reduction in track speeds and directionality as compared with WT T cells (Fig. 2, E–G; and Video 2). Furthermore, Myo9b^{-/-} T cell tracks showed a mild increase in arrest coefficients and broader turning angles compared with WT T cell tracks (Fig. 2, H and I). Yet, the motility coefficient, which is a measure of a cell's ability to scan the environment, remained comparably robust at 40 $\mu\text{m}^2/\text{min}$ for Myo9b^{-/-} T cells (Fig. 2 J). Collectively, Myo9b plays a detectable but unexpectedly minor role during naive T cell trafficking to and within lymphoid tissue.

Myo9b is dispensable for T cell activation and expansion

Because actomyosin contractility has emerged as a central regulator of immunological synapse (IS) formation with DCs (Comrie et al., 2015; Le Floch and Huse, 2015; Hashimoto-Tane et al., 2016; Thauland et al., 2017), we investigated T cell activation parameters of WT and Myo9b^{-/-} T cells. To address cytoskeletal dynamics, we followed T cell spreading on αCD3 -coated plates, followed by fixation and F-actin staining at different time points. Myo9b^{-/-} T cells showed a delayed but ultimately comparable spread on αCD3 -coated plates as WT T cells (Fig. S3, A and B). Similarly, polyclonal T cell proliferation after αCD3 or $\alpha\text{CD3}/\text{CD28}$ mAb stimulation was equivalent between both populations (Fig. S3 C). To analyze antigen-specific responses, we crossed Myo9b^{-/-} mice to OT-I TCR transgenic mice, in which CD8⁺ T cells recognize the OVA_{257–264} peptide in the context of H2-K^b (Kearney et al., 1994). In vitro stimulation with activated DCs pulsed with OVA_{257–264} led to robust proliferation of both WT and Myo9b^{-/-} OT-I T cells over a wide range of peptide concentrations (Fig. S3 D).

We examined whether features present in lymphoid tissue, such as search and arrest at pMHC-presenting DCs, impact on Myo9b^{-/-} CD8⁺ T cell activation. As a computational framework, we modeled in silico encounter frequencies of synthetic WT and Myo9b^{-/-} T cell tracks assembled from intravital imaging data with abundant (10^4) and rare (50) DCs distributed in a sphere of 1 mm in diameter as surrogate T cell area. In line with the modest impact of Myo9b deficiency on the motility coefficient, our modeling predicted that Myo9b^{-/-} T cells showed identical encounter frequencies at abundant DC levels (99.7% vs. 99.6% WT and Myo9b^{-/-} T cells) and only a marginal reduction in encounter frequencies under rare DC conditions (20.3% for WT to 15.1% for Myo9b^{-/-} T cells; Fig. 3, A and B). To experimentally corroborate these data, we transferred 100 nM OVA_{257–264}-pulsed DCs into footpads of mice 18 h before transfer of OT-I and Myo9b^{-/-} OT-I T cells and performed 2PM imaging and flow cytometry analysis.

In agreement with our simulations, experimental 2PM imaging of reactive LNs showed WT and Myo9b^{-/-} OT-I T cells in close apposition to OVA_{257–264}-pulsed DCs (Fig. 3 C and Video 3), with Myo9b^{-/-} OT-I cells showing decreased cell speeds and longer DC interactions as compared with OT-I T cells (Fig. 3, D and E).

Next, we examined whether CD8⁺ T cell differentiation was affected in the absence of Myo9b. WT and Myo9b^{-/-} OT-I T showed a similar expression of the early activation markers CD69 and CD25 (Fig. 3, F and G; and Fig. S3 E). Despite a minor decrease in Myo9b^{-/-} OT-I T cell proliferation at 48 h, OT-I and Myo9b^{-/-} OT-I T cells underwent similar cell proliferation at 72 h after transfer (Fig. 3, H and I). We obtained comparable data when using 1 μM OVA_{257–264}-pulsed DCs (unpublished data). Finally, we quantified WT and Myo9b^{-/-} T cell expansion in a microbial infection model. OT-I and Myo9b^{-/-} OT-I T cells were transferred into GFP⁺ C57BL/6 recipients, which were subsequently infected with an OVA-expressing LCMV strain (LCMV-OVA; Fig. 3 J; Ozga et al., 2016). At 6 and 14 d after infection, we observed comparable expansion of both populations in SLOs including spleen, PLN, and MLN (Fig. 3 K and Fig. S3 F). Collectively, Myo9b^{-/-} T cells interact avidly with DCs and show robust proliferation after in vitro and in vivo stimulation, suggesting that T cell activation is regulated by Myo9b-independent mechanisms.

Myo9b is required for T cell homing to NLT

We hypothesized that the widely spaced SLO architecture (Bajénoff et al., 2006; Novkovic et al., 2016), in combination with the permissive transmigration through high endothelial venules (HEVs; Mionnet et al., 2011) and the lack of postcapillary venules in spleen, may partially compensate for the lack of Myo9b-regulated Rho activity during naive T cell recirculation. In contrast, the switch of effector T cell trafficking to NLT may conceivably impose stricter demands on spatiotemporal orchestration of the actomyosin cytoskeleton, owing to the altered confinement, topology, and barrier structures in these organs (Charras and Sahai, 2014). To perform long-term in vivo observations, we backcrossed WT and Myo9b^{-/-} OT-I mice to fluorescent protein-expressing reporter mice and cotransferred GFP⁺ Myo9b^{-/-} OT-I and dsRed⁺ OT-I T cells into C57BL/6 mice 1 d before skin infection with tdTomato- and OVA-expressing HSV-1 (HSV-1_{TOM-OVA}; Fig. 4 A). In this model, local HSV-1_{TOM-OVA} infection induces the recruitment of effector CD8⁺ T cells that give rise to a T_{RM} population after viral clearance (Ariotti et al., 2015). As in the LCMV-OVA model, expansion and contraction of dsRed⁺ OT-I and GFP⁺ Myo9b^{-/-} OT-I T cells after HSV-1_{TOM-OVA} were comparable between days 8 to 30 in blood, reflected in similarly sized memory populations in spleen and PLN on day 30 after infection (Fig. 4, B and C). In contrast, the recovery of Myo9b^{-/-} OT-I T_{RM} cells from skin was significantly reduced as compared with WT OT-I T cells (Fig. 4 C). We found a similar reduction of Myo9b^{-/-} OT-I T cells in submandibular salivary glands (SMGs), an NLT frequently invaded by expanding effector T cells, on day 30 after HSV-1_{TOM-OVA} infection (Fig. 4 C). A comparable decline of recovered Myo9b^{-/-} OT-I T cells was also observed in SMGs on day 6 and 14 after systemic LCMV-OVA infection (unpublished data). A detailed analysis of HSV-1_{TOM-OVA}-infected skin sections revealed strongly reduced numbers of epidermal Myo9b^{-/-} T_{RM}

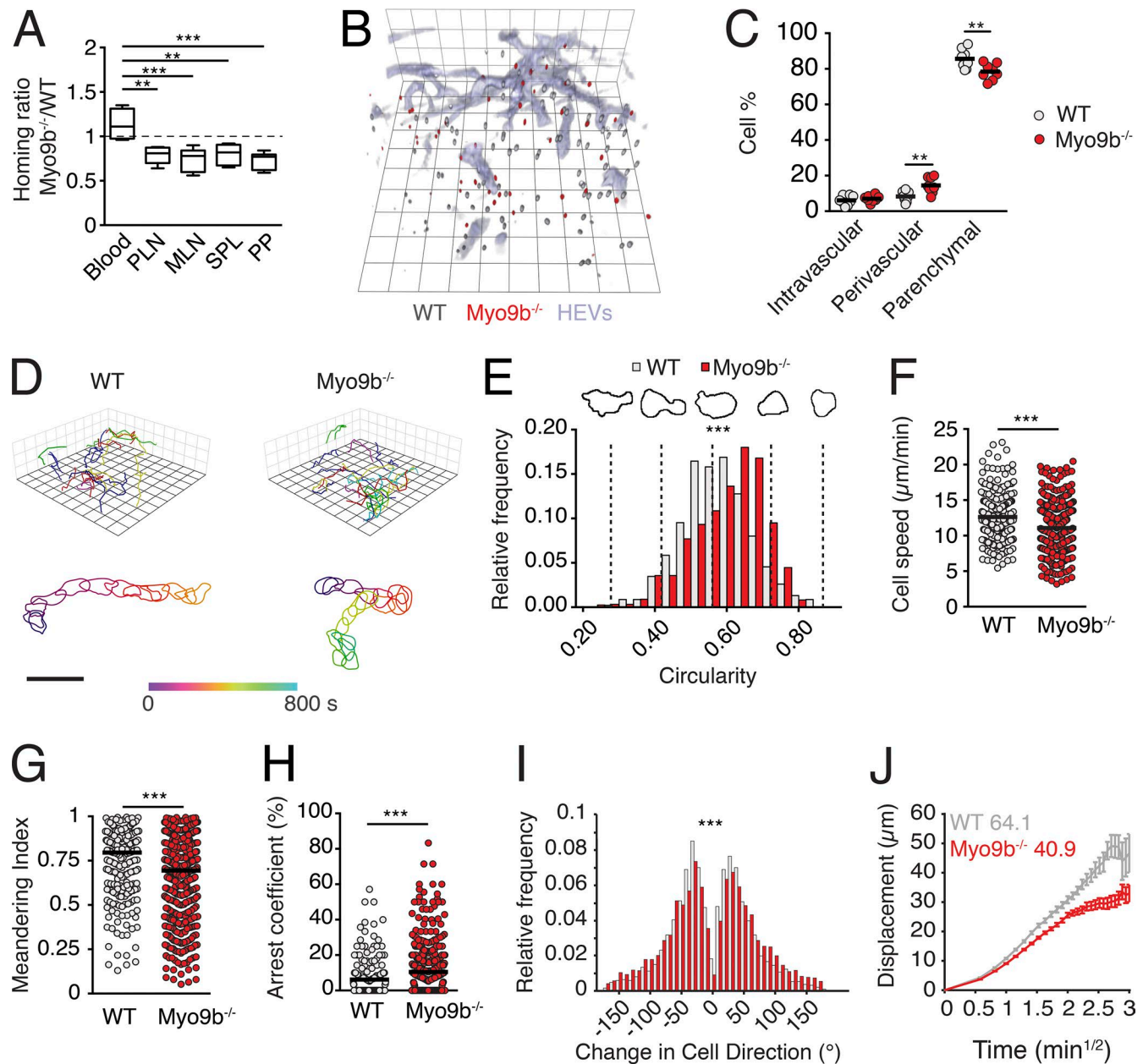


Figure 2. *Myo9b* deficiency causes a mild reduction of in vivo T cell homing and interstitial motility in LNs. (A) Homing ratio of *Myo9b*^{-/-} to WT T cells at 2 h after transfer. Data are pooled from four to six recipient mice of two to three independent experiments. Shown is median with 25 and 75% quartiles and minimum/maximum values. (B) 3DIF LN reconstruction of adoptively transferred WT (gray) and *Myo9b*^{-/-} (red) T cells at 40 min after transfer. HEVs are labeled blue. Square length, 35 μ m. (C) Localization of adoptively transferred WT (gray) and *Myo9b*^{-/-} (red) T cells in LNs as percent of recovered cells. Pooled from two independent experiments. (D) Top, representative 2PM tracks of migrating WT and *Myo9b*^{-/-} T cells in LN interstitium. Square length, 15 μ m. Bottom, representative time-resolved shapes of WT and *Myo9b*^{-/-} T cells. Bar, 20 μ m. (E–J) Quantification of 2PM motility parameters. Pooled from seven image sequences in three independent experiments. Circular frequency analysis (E), mean track speeds (F), meandering index (G), arrest coefficient (H), turning angle distribution (I), and motility coefficient analysis (J) of WT and *Myo9b*^{-/-} T cells in LN interstitium. Horizontal bars in C, F, and G depict mean, whereas horizontal bar in H shows median. Statistical analysis: ANOVA with Tukey's multiple comparison test (A); paired Wilcoxon test (C); Mann-Whitney test (E, G, H, and I); unpaired Student's *t* test (F). **, $P < 0.01$; ***, $P < 0.001$.

as compared with their WT counterparts, whereas there was no significant difference in dermal T cell numbers (Fig. 4, D and E). A similar reduction in epidermal *Myo9b*^{-/-} T cells became already detectable during the effector phase (day 8 after infection), whereas dermal T_{EFF} numbers were slightly increased in the absence of *Myo9b* (Fig. S4). In contrast to the defective NLT homing, *Myo9b*^{-/-} OT-I T cells isolated from tattooed skin and

LN on day 30 showed similar expression of CD127 and lack of KLRG1 as WT OT-I T cells (Fig. 4 F), and both skin T cell populations increased CD103, CD69, and CXCR3 expression (Fig. 4 G). These data support the notion of a largely intact development of adoptively transferred T cells into T_{CM} and T_{RM} cells irrespective of *Myo9b* expression. Collectively, our data indicate that despite their equivalent expansion and frequency in SLOs as WT CD8⁺ T

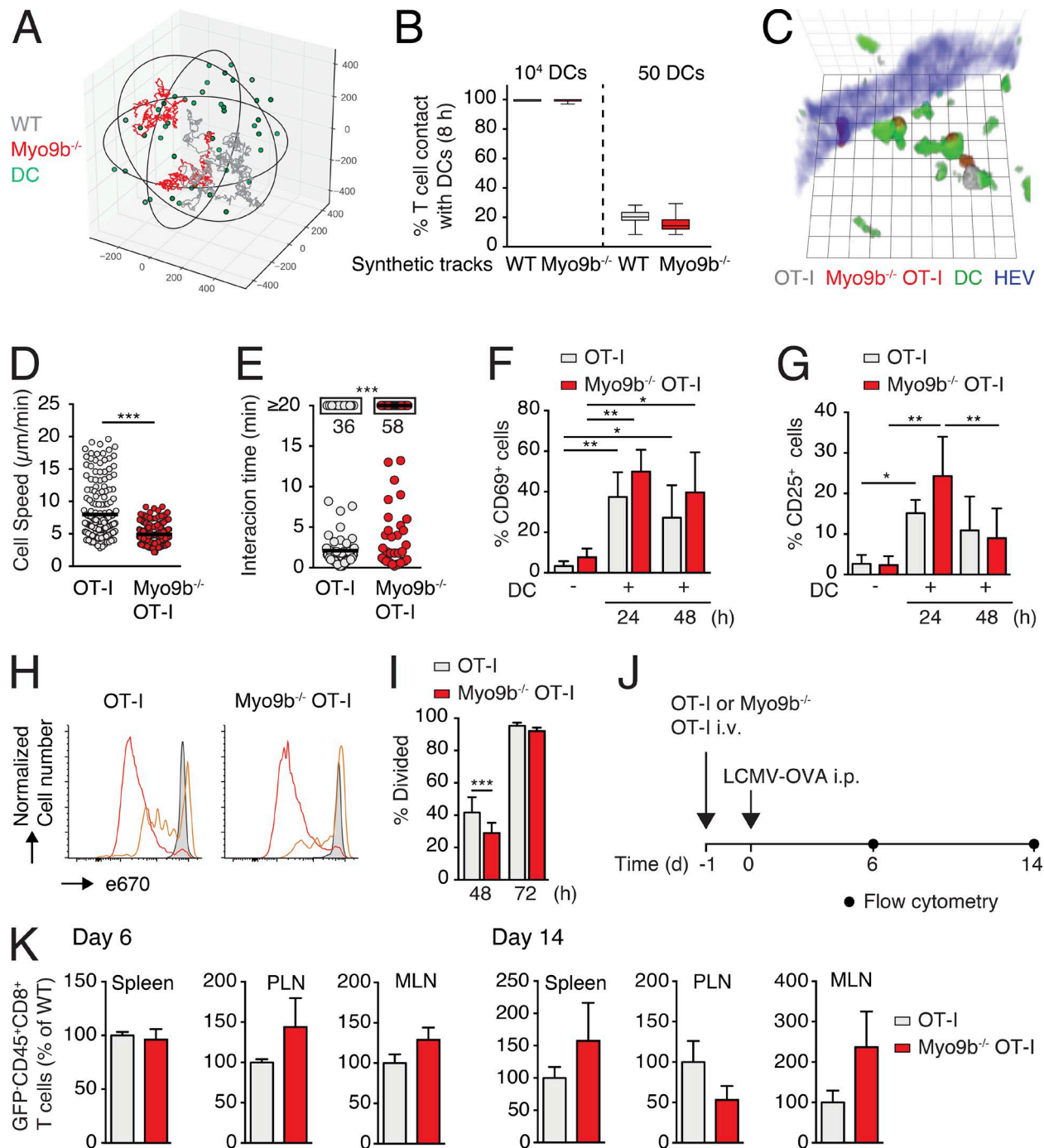


Figure 3. Myo9b is dispensable for T cell activation and expansion. (A) Exemplary synthetic WT (gray) and Myo9b^{-/-} (red) T cell tracks in a 1-mm diameter sphere containing 50 DCs (green). (B) Percentage of synthetic WT and Myo9b^{-/-} T cell contacts with at least one DC at high (10⁴) or low (50) DC densities. 100 synthetic T cell tracks were analyzed over an 8-h period. Shown is median with 25 and 75% quartiles and minimum/maximum values. (C) 2PM image of WT (gray) and Myo9b^{-/-} (red) OT-I T cells interacting with 100 nM OVA₂₅₇₋₂₆₄-pulsed DCs (green). HEVs are depicted blue. Square length, 8 μm. (D and E) Dynamic OT-I T cell–DC interaction parameters. Cell speeds (D) and interactions >30 min (E) of WT and Myo9b^{-/-} OT-I T cells with OVA₂₅₇₋₂₆₄-pulsed DCs. Pooled from four mice in two independent experiments. Horizontal bars in D depict mean and horizontal bars in E show median. (F–K) Activation and proliferation analysis of WT and Myo9b^{-/-} OT-I T cells. Percent CD69⁺ (F) and CD25⁺ (G) WT and Myo9b^{-/-} OT-I T cells at 24 and 48 h, respectively, after T cell transfer into mice containing 100 nM OVA₂₅₇₋₂₆₄-pulsed DCs. Shown is mean ± SD. Pooled from three independent experiments with 4–11 mice per condition. (H) Proliferation of e670-loaded WT and Myo9b^{-/-} OT-I T cells at 0 (gray shade), 48 (orange), and 72 h (red) after transfer. (I) Quantification of percent divided WT and Myo9b^{-/-} OT-I T cells at 48 and 72 h after transfer. Shown is mean ± SD. Pooled from three independent experiments with four to seven mice per condition. (J) Experimental layout of systemic LCMV-OVA infection. (K) Percentage of Myo9b^{-/-} OT-I T cells normalized to WT OT-I T cells at day 6 and 14 after infection (mean ± SEM). Pooled from three independent experiments with six to seven mice per time point. Statistical analysis: unpaired Student's *t* test (D and K); Mann-Whitney test (E); ANOVA between selected columns with Sidak's multiple comparison test (F, G, and I). *, *P* < 0.05; **, *P* < 0.01; ***, *P* < 0.001.

cells, Myo9b^{-/-} T cells are selectively impaired in their accumulation in epithelial barrier tissues.

Myo9b facilitates T cell entry into the epidermal compartment

To examine the impact of Myo9b deficiency on NLT T cell behavior in more detail, we visualized GFP⁺ Myo9b^{-/-} and dsRed⁺ OT-I T_{RM} cells in epidermis of HSV-1_{TOM-OVA}-infected mice at >30 d after infection using 2PM. In line with flow cytometry and immunohistological data, representative 2PM scans showed significantly reduced Myo9b^{-/-} OT-I T_{RM} cell numbers in the epidermal layer as compared with OT-I T_{RM} cells (Fig. 5, A–C), comparable to the reduction seen with CXCR3^{-/-} OT-I T cells (unpublished data; Mackay et al., 2013). We observed similar numbers of cotransferred GFP⁺ versus dsRed⁺ WT OT-I T cells in HSV-1_{TOM-OVA}-infected epidermis, ruling out an influence of fluorescent protein expression on T cell accumulation in skin (unpublished data). Next, we performed time-lapse 2PM image acquisitions in epidermal regions containing relatively high Myo9b^{-/-} OT-I T cell numbers to obtain robust datasets of dynamic motility parameters. Residual epidermal Myo9b^{-/-} OT-I T_{RM} cells showed a more spherical cell shape with fewer protrusions as compared with OT-I T_{RM} (Fig. 5, D and E; and Videos 4 and 5), with some cells spontaneously rounding up as observed in LNs (Fig. 5 M). In accordance, mean membrane protrusion speeds were decreased in epidermal Myo9b^{-/-} OT-I T_{RM} (Fig. 5 F), accompanied by a 30% reduction in cell speeds, as compared with WT OT-I T_{RM} (Fig. 5 G). In contrast, epidermal Myo9b^{-/-} OT-I T cells showed increased directionality as compared with OT-I T cells (Fig. 5 H; and Videos 4 and 5). As a result, in silico generated 24-h-long synthetic tracks modeled from intravital observations predicted a largely preserved ability of Myo9b^{-/-} T cells to scan epidermal tissue (Fig. 5 I). In agreement with the modeling, the epidermal motility coefficient was comparable between WT and Myo9b^{-/-} OT-I T_{RM} (Fig. 5 J). In sum, although Myo9b^{-/-} CD8⁺ T cells were strongly underrepresented in epidermis, Myo9b deficiency had no discernible impact on the tissue scanning ability of residual T cells.

Although we focused on epidermal T cell motility parameters, our image volumes routinely contained dermal regions underlying the epidermal layer, where only few CD8⁺ T cells reside in the memory phase (Gebhardt et al., 2011; Ariotti et al., 2012). In line with immunohistological data (Fig. 4, F and G), 2PM reconstructions consistently showed readily detectable dermal Myo9b^{-/-} OT-I T cells (Fig. 5 K and Video 6). Although dermal Myo9b^{-/-} OT-I T cells showed a slight decrease in cell speeds compared with OT-I T cells (Fig. 5 L), both populations moved considerably faster as compared with epidermal T cells, in agreement with previous observations (Gebhardt et al., 2011). A detailed analysis of 2PM videos uncovered dermal Myo9b^{-/-} OT-I T cells apparently aiming to cross the BM underneath the epidermal cell layer, a behavior we rarely observed for the few dermal OT-I T cells remaining on day 30 after infection (Fig. 5, M and N; and Video 7). Thus, 21 of 23 incomplete dermal–epidermal translocation events (defined by temporary arrest of dermal T cells beneath the T_{RM}-containing epidermal layer) were attempted by Myo9b^{-/-} T cells, whereas only two were observed for WT T cells.

Myo9b facilitates T cell transmigration through high-density ECM barriers

Our results suggested that the control of Rho activity by Myo9b facilitates the crossing of dense ECM barriers by either allowing protrusion formation at the leading edge and/or lowering cell surface stiffness. To directly address this hypothesis, we generated in vitro ECM barriers of different densities on top of Transwell filter inserts, using either laminin, low density (LD), or high-density (HD) collagen preparations. SEM imaging confirmed the increased closing of the 5-μm pores in the order of laminin < LD collagen < HD collagen (Fig. 6 A). We also tested the prototypical BM components laminin 411, laminin 511, and collagen IV, but failed to create a homogeneous layer covering Transwell pores (unpublished data). We then compared the ability of WT and Myo9b^{-/-} T cells to accumulate in response to a CCL21 gradient across ECM barriers. Migration of WT T cells declined with increasing barrier function, but remained clearly detectable even in HD collagen-coated wells (Fig. 6 B). In contrast, we observed an ascending impact of Myo9b deficiency on T cell chemotaxis with increasing barrier density. Although uncoated or laminin-coated filters confirmed the base-line reduction of Myo9b^{-/-} T cell chemotaxis, LD, and, in particular, HD collagen-coating precipitated a marked decrease in the numbers of transmigrated Myo9b^{-/-} T cells (Fig. 6, B and C). Compared with uncoated wells, Myo9b^{-/-} T cells showed a further 52 and 81% reduction in transmigration through LD and HD collagen barriers, respectively. We obtained similar results when we analyzed Myo9b^{-/-} T cell transmigration through the ECM matrix deposited by two epithelial cell lines (Fig. S5). Transmigration of Myo9b^{-/-} T cells through HD collagen-coated Transwell inserts was reestablished by pharmacological inhibition of active Rho and MLCK, but not ROCK and LIMK (Fig. 6 D). Collectively, our in vitro transmigration results uncover a prominent role for Myo9b to allow crossing of dense ECM barriers, resembling the impaired epidermal accumulation of Myo9b^{-/-} T cells in vivo.

Myo9 is required for efficient early control of viral spread in skin

We analyzed whether the reduced efficacy of NLT seeding of Myo9b^{-/-} T cells impaired protection in a local skin infection model. To this end, we examined whether recruitment of T_{CM} cells, which efficiently home to inflamed skin (Osborn et al., 2017), is impaired in the absence of Myo9b. We transferred WT or Myo9b^{-/-} OT-I T_{CM} cells into perforin-deficient (Prf-1^{-/-}) hosts that are unable to efficiently kill virus-infected cells. 1 d later, we challenged Prf-1^{-/-} mice with a local skin infection of HSV-1_{TOM-OVA} and measured viral titers at 60 h after infection (Fig. 7 A; Ozga et al., 2016). WT but not Myo9b^{-/-} OT-I cells significantly decreased viral titers at this time point as compared with Prf-1^{-/-} mice that had not received T cells, suggesting that trafficking to skin early after viral infection is impaired in the absence of Myo9b activity (Fig. 7 B).

Myo9 is required for T_{RM}-mediated global skin immunity

Finally, we investigated how Myo9b affects the function of established T_{RM} populations. In a first set of experiments, we analyzed the TCR responsiveness of epidermal WT and Myo9b^{-/-} OT-I T

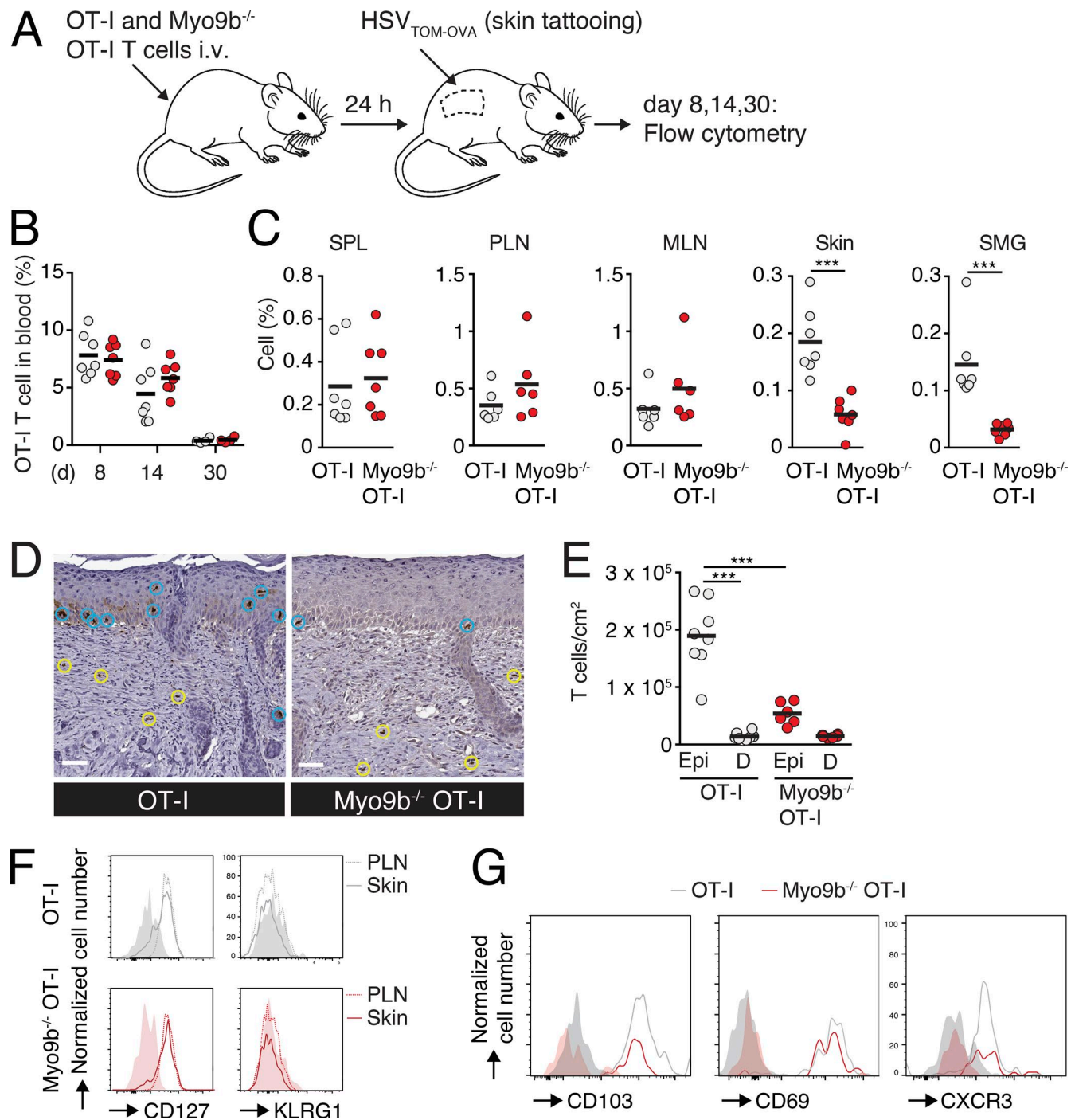


Figure 4. Myo9b is required for T cell accumulation in NLTs. (A) Experimental layout of HSV-1_{TOM-OVA} skin infection. (B) Percentage of WT and Myo9b^{-/-} OT-I T cells in blood on days 8, 14, and 30 after infection. (C) Percentage of WT and OT-I Myo9b^{-/-} T cells (FSC/SSC/singlet gate) in spleen, PLN, MLN, SMG, and skin of HSV-1_{TOM-OVA}-infected mice on day 30 after infection. Each dot represents data from one mouse in two independent experiments. (D) WT and Myo9b^{-/-} OT-I T cells (brown) in epidermis (blue circles) and dermis (yellow circles) on day 30 after infection IHCs were counterstained with Mayer's Hematoxylin. Nuclei are in blue. Bars, 50 μ m. (E) Quantification of WT and Myo9b^{-/-} OT-I T cell distribution per cm² of epidermis (Epi) or dermis (D). Each dot represents one skin section pooled from two independent experiments with three mice and six sections analyzed per genotype. (F) Flow cytometry of activation parameters of WT and Myo9b^{-/-} OT-I T cells on day 30 after infection in PLN and skin. Filled-color histograms are isotype controls. (G) Flow cytometry of activation parameters of WT and Myo9b^{-/-} OT-I T cells on day 30 after infection in skin. Filled-color histograms are FMO controls. Statistical analysis: unpaired Student's *t* test (B and C); ANOVA between selected columns with Sidak's multiple comparison test. ***, *P* < 0.001. Horizontal bars depict mean.

cells created after HSV-1_{TOM-OVA} skin infections. To this end, we administered OVA₂₅₇₋₂₆₄ peptide in situ and followed T cell shape changes by 2PM as surrogate readout for TCR signaling (Ariotti

et al., 2012). Epidermal Myo9b^{-/-} OT-I T_{RM} cells displayed a similar rounding and motility arrest as WT OT-I T cells after peptide stimulation (Fig. 8, A–C). Furthermore, WT and Myo9b^{-/-} OT-I

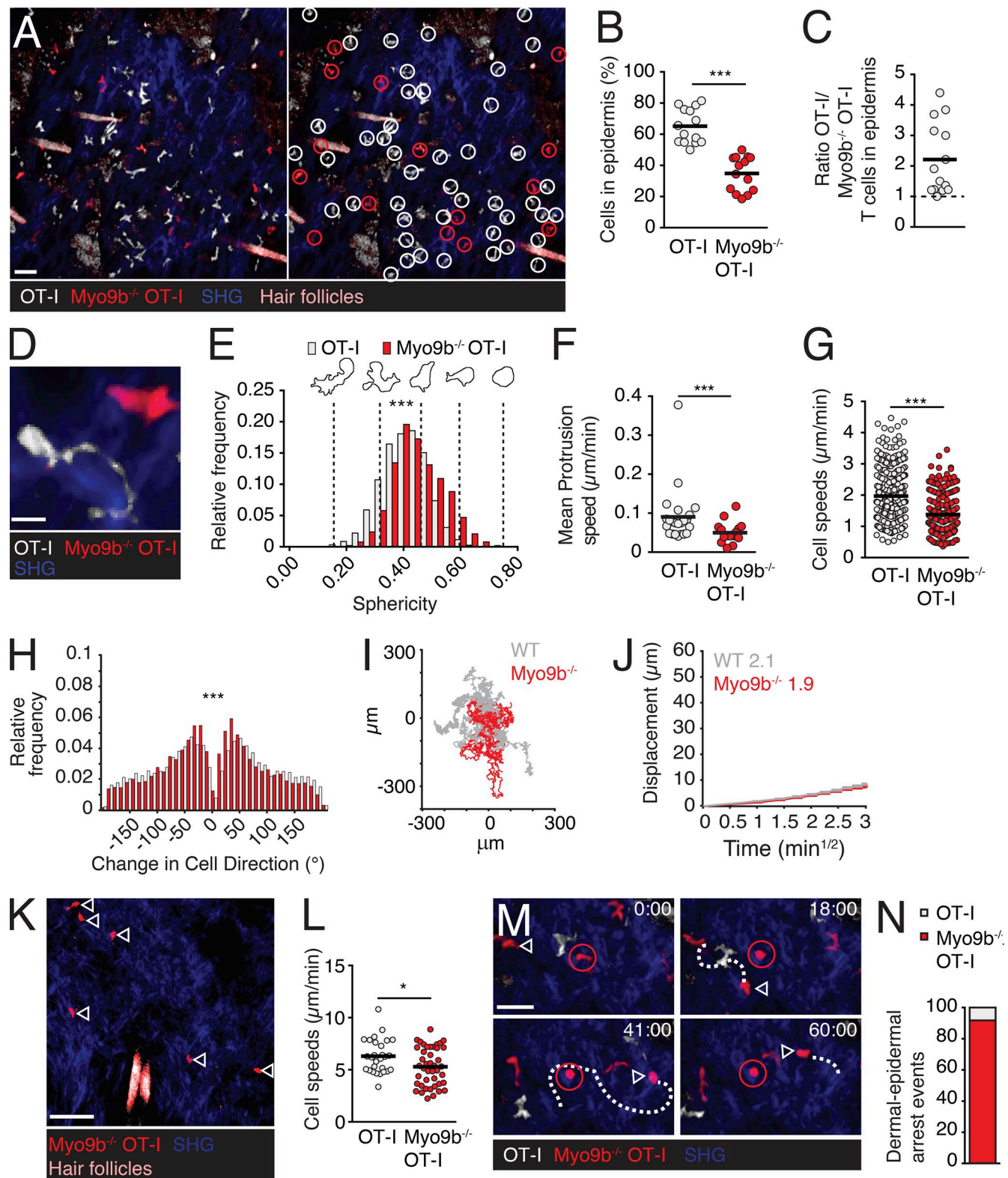


Figure 5. Myo9b is required for dermal T cell entry into epidermis. (A) 2PM image of dsRed⁺ OT-I and GFP⁺ Myo9b^{-/-} OT-I T cells in skin on day 30 after HSV-1_{TOM-OVA} infection. The right panel identifies individual OT-I (white circles) and Myo9b^{-/-} (red circles) OT-I T cells. (B) Percentage of WT and Myo9b^{-/-} OT-I T cells per field of view. (C) Ratio of WT and Myo9b^{-/-} OT-I T cells in epidermal layer. Each dot represents one field of view collected from six mice in two independent experiments. Dotted line represents equal number of OT-I versus Myo9b-deficient OT-I T cells in a field of view. (D) 2PM image of OT-I and Myo9b^{-/-} OT-I T cell. (E-H) Dynamic motility parameters in epidermis. Sphericity (E), mean protrusion speed (F), single cell speeds (G), and turning angles (H) of epidermal OT-I and Myo9b^{-/-} OT-I T cells. (I) Exemplary synthetic WT (gray) and Myo9b^{-/-} (red) T cell tracks derived from 2PM datasets and projected over a 24-h period. (J) Motility coefficient of epidermal OT-I and Myo9b^{-/-} OT-I T cells. (K-N) Dynamic motility parameters in dermis. (K) 2PM image of dermal T cells (>25 μ m below the epidermal T_{RM} layer). Arrowheads depict Myo9b^{-/-} OT-I T cells. (L) Single cell speeds of dermal OT-I and Myo9b^{-/-} OT-I T cells. (M) 2PM image of

T_{RM} cells sorted from skins of HSV-1_{TOM-OVA}-infected mice showed comparable in vitro cytotoxicity against OVA₂₅₇₋₂₆₄-pulsed target cells (Fig. 8 D), suggesting equivalent TCR activation and cytotoxic capacity. To assess the protective function of T_{RM} populations in the absence of Myo9b, we generated skin-resident OT-I T cells phase by tattooing OVA₂₅₇₋₂₆₄ peptide onto the skin of Prfl^{-/-} mice at day 3 after infection with LCMV-OVA (Fig. 8 E). Tattoo-induced skin inflammation led to T_{EFF} recruitment and local cognate antigen increases T_{RM} generation (Mackay et al., 2012; Khan et al., 2016). On day 30 after infection with LCMV-OVA, we challenged sensitized as well as contralateral skin sections with HSV-1_{TOM-OVA} in presence of the SIP1 antagonist FTY720 to prevent recruitment of circulating effector/memory T cells (Pan et al., 2017). At 60 h after infection with HSV-1_{TOM-OVA}, we determined viral titers in sensitized and contralateral skin. OVA₂₅₇₋₂₆₄-sensitized skin of WT OT-I T cell recipients showed significantly lower viral titers as compared with untreated Prfl^{-/-} mice that served as control for maximal viral titers. Of note, the contralateral skin of mice that had received WT OT-I T cells also showed decreased viral titers, in line with a global immunity provided by skin-resident T_{RM} (Fig. 8 F; Jiang et al., 2012). In OVA₂₅₇₋₂₆₄-sensitized skin of Myo9b^{-/-} OT-I T cell recipients, we observed a comparable reduction in HSV-1_{TOM-OVA} titers as in sensitized skin of WT OT-I recipients. This result suggests that despite reduced skin homing, cognate peptide tattooing resulted in sufficient recruitment and expansion of Myo9b^{-/-} CD8⁺ T cells to form a residual T_{RM} population. In contrast, Myo9b^{-/-} T cells failed to provide global skin immunity because the contralateral side showed no decrease of HSV-1_{TOM-OVA} titers as compared with nonimmunized Prfl^{-/-} mice (Fig. 8 F). Thus, our data support a pivotal role for Myo9b to endow effector T cells the ability to enter and persist in NLTs for global host protection, in addition to impaired early antiviral responses (Fig. 7).

Discussion

Activation of CD8⁺ T cells triggers their switch from a SLO- to an NLT-trafficking pattern. In NLTs, effector T cells eliminate viral reservoirs and establish protective memory T cell populations. Numerous studies have identified adhesion molecules, chemokine receptors, and tissue-specific cues allowing effector T cell recruitment and T_{RM} development (von Andrian and Mackay, 2000; Schenkel and Masopust, 2014; Nolz, 2015; Mueller and Mackay, 2016). In contrast, it remains poorly understood how dynamic regulation of the actomyosin cytoskeleton supports the remarkable adaptation of effector T cells to NLT microenvironments. Our data show that, despite minor defects in SLO trafficking patterns, Myo9b^{-/-} CD8⁺ T cells retained central features of T cells, such as encounter and interaction with cognate pMHC-presenting DCs and expansion after stimulation. In contrast, lack of

Myo9b led to a striking inhibition of CD8⁺ T cell accumulation in NLTs that strongly correlated with defects in BM barrier-crossing capacity. One conceivable explanation for this phenotype is that reduced protrusion formation, correlating with increased cell surface stiffness, impairs Myo9b^{-/-} T cell seeding of NLTs during the effector phase, whereas SLOs with permissive HEVs and widely spaced fibroblast networks are successfully surveilled by these cells. These data also support the notion of significant differences in the physical constraints imposed on motile T cells in lymphoid versus nonlymphoid tissues, although this needs to be further explored in future experiments.

>70 GEFs and 60 GAPs regulate small GTPase activity, and many of them are expressed in leukocytes (Tybulewicz and Henderson, 2009). Yet, there is scarce information on how regulation of small GTPase activity through GEFs and GAPs impacts on the distinct stages of T cell responses in SLOs and NLTs. The high expression levels of Myo9b in naive and effector/memory CD8⁺ T cells prompted us to use AFM to examine its impact on cell surface mechanics in the absence of chemotactic stimulation. The median value of the Young's modulus of 0.15 kPa allocates CD8⁺ T cells to the lower end of the cell stiffness scale, which ranges from ~0.1 kPa to >10 kPa in fibroblasts (Alonso and Goldmann, 2003). Similar values were previously reported for human T cells using micropipette-aided microindentation or stepwise compression between two parallel plates, suggesting that lymphocytes regulate the mechanical properties of their cell surface within a narrow range (Bufi et al., 2015; Guillou et al., 2016). In the absence of chemokine stimulation, Myo9b^{-/-} CD8⁺ T cells showed a 30% increase in the median Young's modulus, presumably owing to augmented cell cortex contraction by actomyosin filaments. Although this increase is small as compared with differences in Young's modulus between distinct cell types, in vitro migration data support a close correlation of increased cell surface stiffness with impaired motility. This was unexpected, because increased Rho-ROCK-Myosin II-mediated contractility induces polarity and spontaneous motility in neutrophils and other cell types, therefore playing a pro- rather than antimigratory role (Niggli, 2003; Xu et al., 2005; Ruprecht et al., 2015; Vargas et al., 2016). A likely explanation for this discrepancy is the directed activity of Myo9b at the leading edge for local suppression of Rho activity (Hanley et al., 2010), thereby facilitating protrusion formation by Rac and Cdc42. Thus, although Rho-mediated contractility at the uropod is central to leukocyte motility in 3D environments, our data suggest that its activity at the leading edge must be contained for optimal migration. After CCL21 stimulation, pMLC levels were further increased in Myo9b^{-/-} T cells and the cells were less polarized than their WT counterparts. This indicates that Myo9b regulates both basal and chemokine receptor-triggered Rho-GTP levels that control cell surface elasticity and protrusive activity. Inhibition of Rho-GTP rapidly reversed the

failed translocation event of a dermal Myo9b^{-/-} OT-I T cell (arrowhead). The red-circled cell represents a spontaneously rounding epidermal Myo9b^{-/-} OT-I T cell. Time in min and s. (N) Quantification of attempted epidermal translocation events of dermal WT and Myo9b^{-/-} OT-I T cells compiled from eight image sequences in three independent experiments. Mean protrusion rates at the cell periphery were collected from three image sequence movies of two different experiments. Statistical analysis: (B) paired Student's *t* test; (F, G, and L) unpaired Student's *t* test; (E and H) Mann-Whitney test. *, *P* < 0.05; **, *P* < 0.01; ***, *P* < 0.001. Horizontal bars depict mean. Bars: 30 μm (A); 10 μm (D); 40 μm (K); 20 μm (M).

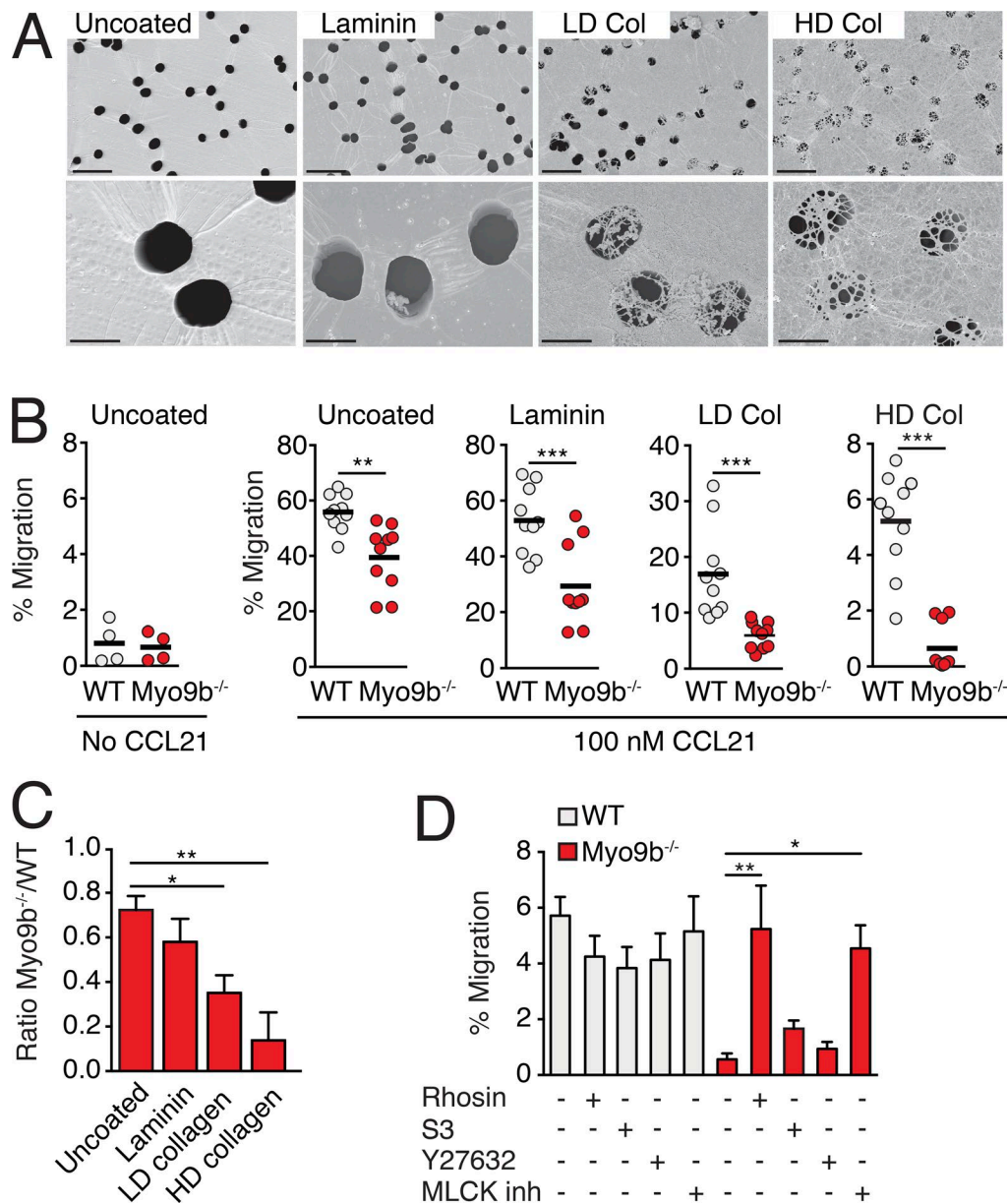


Figure 6. Myo9b facilitates T cell transmigration through increasingly tight ECM barriers. (A) Scanning electron micrographs of uncoated, laminin, LD, and HD collagen-coated Transwell filters with 5- μ m pore size. Bars: 20 μ m (top row); 5 μ m (bottom row). **(B)** Chemotactic migration as percent of input of WT and Myo9b^{-/-} T cells in uncoated and coated Transwell filters. Pooled from three independent experiments. Horizontal bars depict mean. **(C)** Normalized ratio of WT and Myo9b^{-/-} T cell migration through uncoated and coated Transwell filters. Shown is mean \pm SEM. **(D)** Chemotactic migration as percentage of input through HD collagen-coated Transwell filters in presence of indicated inhibitors. Pooled from three independent experiments. Shown is mean \pm SEM. Statistical analysis: unpaired Student's *t* test (B); ANOVA against "uncoated" and "untreated", respectively, with Dunnett's multiple comparison test (C and D). *, *P* < 0.05; **, *P* < 0.01; ***, *P* < 0.001.

migration defect in Myo9b-deficient T cells. Similarly, MLCK inhibition reestablished the chemotactic response of Myo9b^{-/-} T cells, in agreement with its accumulation at the leading edge of polarized T cells (Smith et al., 2003). In addition to regulating cell spreading, increased RhoA activity impairs vesicle transport to the cell surface of activated T cells by strengthening cortical actin networks (Johnson et al., 2012), thereby potentially inhibiting secretion of ECM-degrading enzymes (Prakash et al., 2014). Although this does not account for the basal defect in directed motility of naive Myo9b^{-/-} T cells across uncoated or ECM-coated Transwell filters, we cannot exclude a role for this process in

defective T_{EFF} accumulation in the epidermis. Yet, the observation that Granzyme B-dependent cytotoxicity of Myo9b^{-/-} T_{RM} was comparable to WT T cells suggests that vesicle fusion was not strongly impaired in the absence of Myo9b. Furthermore, WT and Myo9b^{-/-} T_{EFF} showed similar surface levels of LAMP-1, a marker for degranulation on lymphocytes, after in vitro activation (unpublished data).

Naive Myo9b^{-/-} T cells retained robust motility in lymphoid tissue that is made up of a widely spaced FRC scaffold filled with DCs, lymphocytes, and other cells. Thus, the lymphoid microenvironment ameliorated the migratory defect observed in vitro.

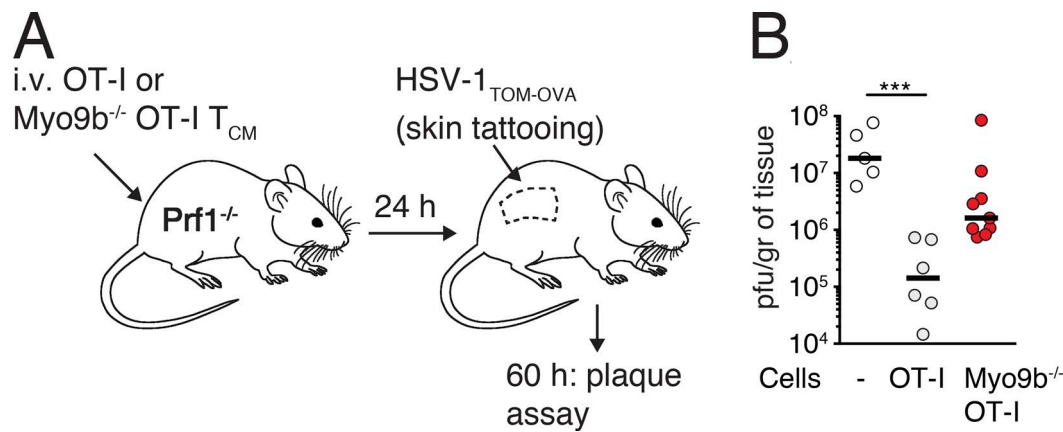


Figure 7. Myo9b is required for early protection in a local skin infection model. (A) Experimental setup of local HSV-1_{TOM-OVA} infection model with OT-I and *Myo9b^{-/-}* OT-I T_{CM} transfer (5×10^5 /mouse) in *Prf1^{-/-}* mice. (B) Viral skin titers at 60 h after infection after transfer of no cells, WT, or *Myo9b^{-/-}* OT-I T_{CM}. Each dot represents skin viral titers from one mouse. Bar depicts median. Data were pooled from two experiments and analyzed using a Kruskal Wallis test against “no cells” with Dunn’s multiple comparison test. ***, $P < 0.001$. Horizontal bars depict mean.

In line with this, recent reports showed that a mild degree of confinement has a promigratory impact on in vitro cell motility through frictional force transmission of the actomyosin cortex to substrates with low adhesiveness (Liu et al., 2015; Ruprecht et al., 2015). Although ICAM-1 is highly expressed in the lymphoid microenvironment, lack of LFA-1-ICAM-1 interactions has only a minor effect on T cell motility parameters in vivo (Woolf et al., 2007; Boscacci et al., 2010), indicating that T cell adhesiveness in SLOs is likely to be low in the absence of TCR signaling and shearing. Consistent with the largely preserved *Myo9b^{-/-}* T cell motility in lymphoid tissue, *Myo9b* deficiency did not preclude T cell-DC encounters, but rather stabilized their interactions. This may be a result of the decreased responsiveness of *Myo9b^{-/-}* T cells to promigratory chemokines such as CCL21, which have been reported to exert a disruptive effect on T cell attachment to DCs (Dustin, 2004). During interactions with DCs, IS formation in T cells is characterized by centripetal F-actin flow important for the proper localization of TCR microclusters (Dustin and Depoil, 2011). Recent studies have uncovered that Rho-triggered actin filament nucleation by formins plays an important role in this process (Murugesan et al., 2016; Hui and Upadhyaya, 2017). Furthermore, changes in cytoskeletal rigidity affect IS size and early TCR signaling in CD4⁺ T cells (Thauland et al., 2017). Nonetheless, in the experimental settings used here, *Myo9b^{-/-}* CD8⁺ T cells showed comparable activation marker up-regulation, proliferation, acquisition of cytotoxic effector functions, and T_{CM} differentiation as WT CD8⁺ T cells. This suggests that additional factors regulate Rho activity at the IS interface, such as Fam65b (Froehlich et al., 2016).

In contrast to the preserved scanning and effector differentiation, we observed a striking defect of *Myo9b^{-/-}* CD8⁺ T cell accumulation in NLTs. NLTs are typically composed of a “functional” parenchymal compartment, consisting of epithelial structures, such as secretory acini of salivary glands or the epidermal layer in skin, and “supportive” interstitial compartments, containing connective tissue, blood and lymph vessels, and innervation. We detected similar numbers of dermal *Myo9b^{-/-}* T cells as compared with WT T cells during the

effector and memory phase, suggesting that the BM surrounding postcapillary venules in nonimmunoprivileged tissues only causes a minor delay in *Myo9b^{-/-}* T cell recruitment. In line with this, imaging studies of inflamed endothelial BM have identified regions of relatively low ECM deposition as preferential exit points for transmigrating leukocytes (Wang et al., 2006). Such permissive structures may mitigate the barrier-crossing defects of *Myo9b^{-/-}* T cells. In contrast, epidermal T cell accumulation was perturbed in the absence of *Myo9b*. Interstitial and parenchymal compartments are separated by tissue-specific, 50- to 300-nm thick BMs that serve as structural scaffold for endothelial and epithelial layers and consist of self-assembling collagen IV and laminin networks cross-linked by nidogens and perlecan (Rowe and Weiss, 2008; Sorokin, 2010). During normal tissue surveillance, billions of leukocytes traverse BMs each day without apparent proteolytic degradation, suggesting the involvement of an actomyosin-driven force generating mechanism (Huber and Weiss, 1989; Rowe and Weiss, 2008; Sorokin, 2010). Yet, the requirements imposed on the actomyosin cytoskeleton for successful transition of BM barriers versus navigation through interstitial and parenchymal compartments have not been comprehensively examined under physiological conditions. Our data suggest that control of cell surface elasticity and concomitant protrusion formation by *Myo9b* is most critical when T cells traverse BM barriers separating spatially confined tissue compartments. We hypothesize that this is a result of the requirement to protrude thin filopodia or pseudopods through gaps in the BM matrix to clear a path for the larger organelles of the cell, in particular the nucleus (Nourshargh et al., 2010; Wolf et al., 2013; Paluch et al., 2016). Our controlled in vitro transmigration experiments indicate that T cell crossing of BM-like structures requires *Myo9b*-mediated suppression of Rho activity, with an inverse correlation to the density of the ECM barrier. In contrast, although T cell motility and shape parameters depend on whether cells migrate in connective or epithelial tissues, T cell motility within a cell matrix is less dependent on localized suppression of Rho function by *Myo9b*. Conceivably, T cells migrating within a cell matrix may

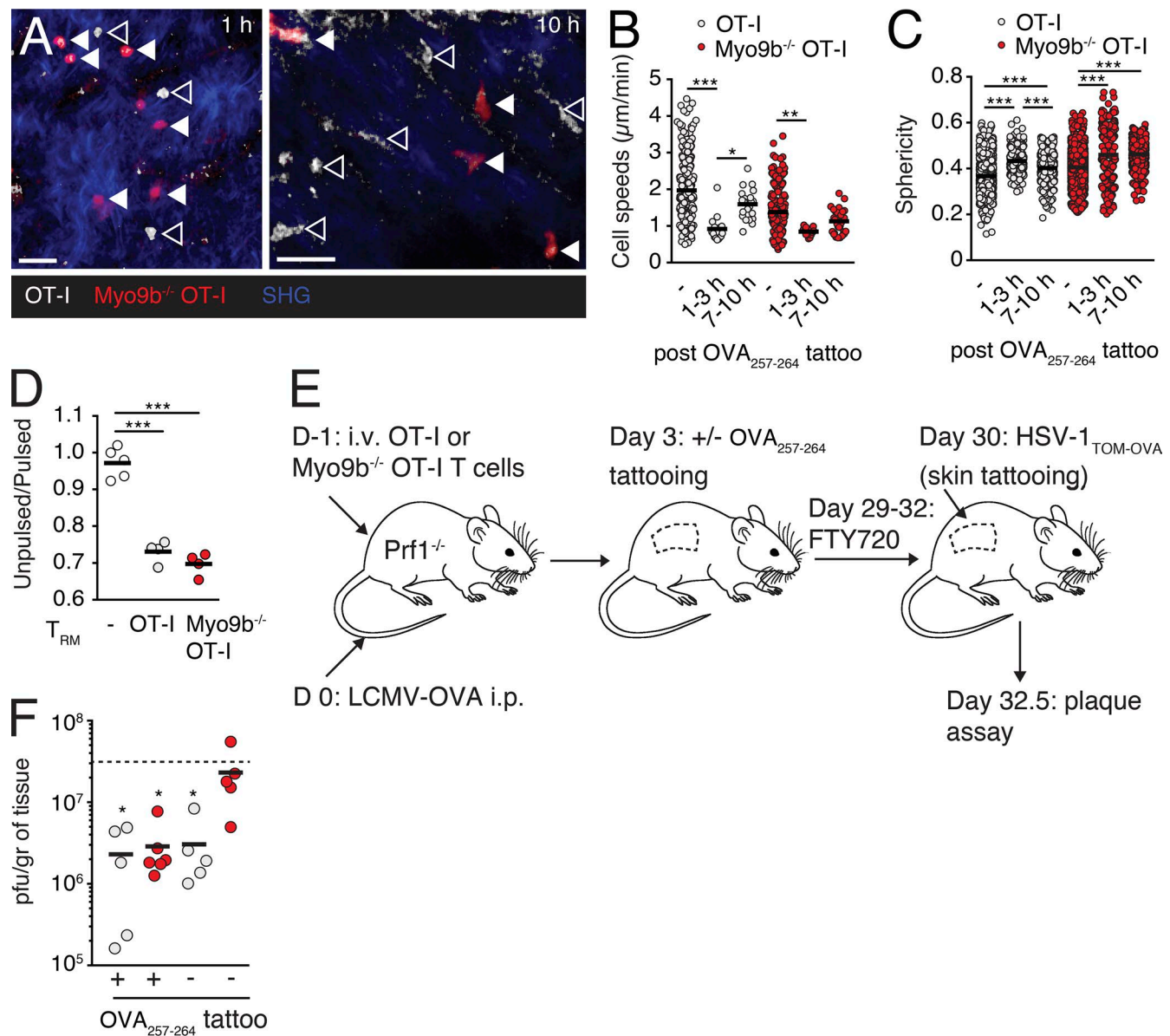


Figure 8. Myo9 enables T cell-mediated global skin immunity. (A) 2PM images of WT (closed arrowheads) and *Myo9b*^{-/-} (open arrowheads) OT-I T_{RM} at indicated time after OVA₂₅₇₋₂₆₄ peptide tattooing. Bars, 20 μm. (B and C) Quantification of 2PM data pooled from six image sequences in two mice from one experiment. WT and *Myo9b*^{-/-} OT-I T_{RM} speeds (B) and sphericity (C) at indicated time after OVA₂₅₇₋₂₆₄ peptide tattooing. (D) In vitro killing efficacy of sorted WT and *Myo9b*^{-/-} OT-I T_{RM}. Pooled from two independent experiments. (E) Experimental strategy to generate WT and *Myo9b*^{-/-} T cells in skins of *Prf1*^{-/-} mice, followed by HSV-1_{TOM-OVA} challenge. (F) Viral titers at 60 h after infection with HSV-1_{TOM-OVA} after transfer of WT or *Myo9b*^{-/-} OT-I T cells in OVA₂₅₇₋₂₆₃-tattooed and untreated contralateral skin flank. Each dot represents skin viral titers from one mouse. Pooled from two experiments. The dotted line corresponds to viral titers after "no cell" transfer (i.e., untreated *Prf1*^{-/-} mice). Statistical analysis: ANOVA with Tukey's multiple comparison test (B and C); ANOVA (D); Kruskal Wallis test against "no cells" with Dunn's multiple comparison test (F). *, P < 0.05; **, P < 0.01; ***, P < 0.001. Horizontal bars depict mean.

experience comparable resistance from all directions, whereas BM may constitute a high resistance barrier. According to this model, interstitially migrating T cells generally choose the path of "least tissue resistance" through formation of new F-actin protrusions away from obstacles such as BM detected by Myo1g and other sensors (Gérard et al., 2014). As consequence, crossing of ECM barriers requires actin polymerization-driven transformation of chemoattractant gradients into mechanical work, thus overcoming the intrinsic propensity of T cells to choose the path of least tissue resistance. A prime example is

the requirement of CXCR3 ligand expression by keratinocytes for efficient epidermal seeding of CD8⁺ T cells (Mackay et al., 2013). Consistent with the barrier function of BM, stromal ECM structures have been shown to reduce T cell infiltration into human tumors (Salmon et al., 2012). This raises the interesting option to modulate T cell infiltration capacity for adoptive cell transfer therapies in cancer immunotherapy, e.g., by increasing their likelihood to cross stromal barriers through actomyosin adaptation. In this context, modulation of Rho signaling pathways in cytotoxic T cells has been recently associated with

improved tumor eradication, although it remains an open issue whether this correlated with improved CD8⁺ T cell infiltration into tumors (Zhou et al., 2014). Additional experiments are needed to gain a more comprehensive picture of the precise constraints exerted by ECM barriers at distinct tissue sites, e.g., by measuring their physical properties and recreating key features in reductionist in vitro models.

T_{RM} play an important role for host defense by seeding NLTs exposed to microbes, such as lung, gastrointestinal tracts, skin, and the mucosal surfaces of the reproductive track (Shin and Iwasaki, 2012; Schenkel and Masopust, 2014; Iijima and Iwasaki, 2015; Mueller and Mackay, 2016). Upon exposure to cognate peptide, T_{RM} generated in previous infections induce a state of tissue-wide alert, effectively blocking viral or bacterial replication (Ariotti et al., 2014; Schenkel et al., 2014; Steinbach et al., 2016). Our data show that in addition to sensitized areas, remote skin areas are also seeded by WT T cells, albeit likely in much lower numbers (Gebhardt and Mackay, 2012), to provide global skin immunity (Jiang et al., 2012). Although T cell differentiation and cytotoxic activity were not impaired in the absence of Myo9b, Myo9b^{-/-} CD8 T cells failed to seed epithelial barrier tissues in large numbers. Nonetheless, in acutely inflamed skin and in the presence of cognate antigen, sufficient Myo9b^{-/-} T_{EFF} cells expanded and differentiated to T_{RM} to provide protection against a local viral reinfection. In contrast, our data suggest that homing of Myo9b^{-/-} T_{EFF} to nonsensitized skin was too low to yield a protective T_{RM} population. Collectively, our observations support a scenario where, in case of strong inflammation (caused here by systemic LCMV infection combined with skin tattooing), proinflammatory signals in serum such as TNF- α or IL-1 trigger a general increase in endothelial cell adhesiveness that allow WT T_{EFF} to disseminate into numerous NLTs for systemic T_{RM} generation (Kadoki et al., 2017). T_{RM} accumulation is most effective in acutely inflamed tissue (e.g., tattooed skin) and when local antigen boosts their numbers (Khan et al., 2016). The tissue protection afforded by Myo9b^{-/-} T_{RM} in sensitized skin areas suggests that limited numbers of epidermal T cells are sufficient to induce a tissue-wide state of alert during pathogen reemergence. Thus, in addition to the reported increasing efficacy of T_{RM} seeding at distal (noninflamed) skin sites after multiple infections (Davies et al., 2017), the degree of T_{RM} protection at distal sites may represent a graded response depending on the degree of general inflammation induced during priming. According to this model, strong systemic inflammatory signals contribute to the generation of an above-threshold protective T_{RM} population at remote skin sites, whereas weaker ones do not. Finally, our data are consistent with a scenario where epithelial BM serves as a physical barrier to contain transmigrated effector T cells in NLT niches and allow them to become T_{RM} through changes in expression of transcription factors, chemoattractant receptors, and integrins (Mueller et al., 2013; Schenkel and Masopust, 2014; Mackay and Kallies, 2017).

In sum, our data define a role for coordinated actomyosin activity to allow effector CD8⁺ T cells to cross ECM barriers in NLTs, leading to establishment of protective populations. Regulation of the actin cytoskeleton is emerging as a critical factor for fine-tuning of tissue-specific adaptive immune responses.

Materials and methods

Mice

Myo9b^{tm1.2Bah} “Myo9b^{-/-}” mice (Hanley et al., 2010) were backcrossed to OT-I TCR transgenic mice (Hogquist et al., 1994) and Tg(UBC-GFP)30Scha “Ubi-GFP” mice (Schaefer et al., 2001). OT-I mice were backcrossed to hCD2-dsRed (Kirby et al., 2009) or Ubi-GFP mice. *Prfl*-deficient and CD45.1 mice were provided by the Institut für Labortierkunde, University of Zürich, Zurich, Switzerland. C57BL/6 mice were purchased from Janvier (AD Horst). All mice were maintained in SPF conditions at the Department of Clinical Research animal facility of the University of Bern, Bern, Switzerland or at the Theodor Kocher Institute, Bern, Switzerland. All animal work has been approved by the Cantonal Committee for Animal Experimentation and conducted according to federal guidelines.

Reagents

Y27632, Rhosin (G04; Shang et al., 2012) and the MLCK inhibitor peptide 18 (MLCK inh) were purchased from CalBioChem. The LIMK inhibitor S3 was from Anaspec. CCL21, CCL19, and CXCL12 were provided by PeproTech, and CXCL13 was from R&D Systems. CFSE, 5-chloromethylfluorescein diacetate (CMFDA; CellTracker green), 7-amino-4-chloromethylcoumarin (CMAC; CellTracker blue), and (5-(and-6)-(((4-chloromethyl)benzoyl)amino) tetramethylrhodamine; CMTMR; CellTracker orange) were purchased from Molecular Probes. Anti-PNAd mAb (MECA-79) was affinity purified from hybridoma supernatant (Nanotools) and fluorescently conjugated using Alexa Fluor protein-labeling kits (Molecular Probes and Invitrogen). For intracellular staining for active RhoA, Fc receptors were blocked with purified anti-CD16/CD32 mAb (2.4G2) in FACS buffer (PBS with 1% FCS and 0.05% NaN₃) for 10 min. Cells were fixed, permeabilized with Cytofix/CytoPerm (Becton Dickinson) for 20 min at 4°C, and stained with anti-active RhoA mAb from NewEast Biosciences in Permashield for 30 min.

Lymphocyte purification

PLN and spleens from wild type and 4- to 8-wk-old Myo9b^{-/-} mice were harvested and homogenized using a 70- μ m cell strainer. Total or CD8⁺ T cells and B cells were isolated using EasySep Negative Selection kits, as described in the manufacturer's instructions (STEMCELL Technologies). Cell purities were typically >95%.

AFM

Cell stiffness was measured using a CellHesion 200 from JPK mounted on an inverted Nikon Ti microscopy. Novascan cantilevers with a 5- μ m borosilicate bead attached and a nominal spring constant of 10 pN/nm were used in all experiments. The actual spring constant of each cantilever was determined by thermal calibration in air. Cantilevers were coated with FBS for ≥ 1 h, followed by a coating with 1% Pluronic (P2443, Sigma) to avoid adhesion to the cells. Measurements were done in fluid. Approach velocity was optimized as 0.5 μ m/s to ensure the fastest rate of elastic measurement without viscoelastic deformation. Retraction speed, which does not affect elasticity measurements, was set to 20 μ m/s. Cells were plated on a Poly-L-Lysine-coated

dish for an hour at 37°C for attachment and thoroughly washed before measurements. The cantilever was positioned at the desired position by bright field microscopy. Each measurement was taken 4–5 times without moving the cantilever in xy and averaged. Young's Modulus of elasticity was calculated by fitting the cantilever deflection versus piezo extension curves to the modified Hertz model as described (Rosenbluth et al., 2006), using the JPK Data Processing software.

Lymphocyte polarization assay

5×10^5 WT and Myo9b^{-/-} purified T cells were plated on top of Fibronectin (10 µg/ml, 200 µl, 3 h at 37°C)-coated coverslips. Cells were stimulated with 100 nM CCL21 and incubated 1 h at 37°C. T cells were fixed with 4% paraformaldehyde (PFA) for 20 min at room temperature, permeabilized in Cytofix/CytoPerm (Becton Dickinson) for 20 min, blocked in Perm Wash/1% BSA for 5 min and labeled with FITC-Phalloidin (Molecular Probes) and DAPI (1 µg per sample, 1 h room temperature in the dark). In some cases, immunostaining was performed with biotinylated anti-CD44 mAb (BioLegend) or PKCζ mAb (Santa Cruz Technology), followed by labeling with Alexa Fluor 488-conjugated streptavidin or Alexa Fluor 555-conjugated anti-rabbit pAb, respectively (Invitrogen). Fluorescence and phase-contrast images were taken with a Zeiss AxioObserver microscope equipped with an Apotome, using a 40× objective. T cell length and width were measured using Zeiss imaging software and expressed as polarity index (i.e., ratio of length to width of the cell).

TCR- and chemokine-induced actin rearrangements

10^5 total lymphocytes from WT or Myo9b^{-/-} mice were plated onto cover glasses in 200 µl medium. To analyze TCR-induced actin rearrangements cover glasses were coated with anti CD3ε antibody (1 µg per sample, 3 h at 37°C) before plating of 10^5 WT or Myo9b^{-/-} lymphocytes. Cells were fixed with 4% PFA at 2, 5, or 10 min after plating. For chemokine-induced actin ruffle formation, cover glasses were coated with Poly-L-Lysine (Sigma). After plating of 10^5 WT or Myo9b^{-/-} lymphocytes, cells were stimulated with 100 nM CCL21 for 20 min, followed by fixation in 4% PFA for 20 min. Cells were washed with PBS, permeabilized with 0.1% Triton/PBS (5 min at room temperature) and labeled with FITC-Phalloidin and DAPI. Cover glasses were washed and mounted with FluorSave (Calbiochem). Cells were scanned by confocal microscopy (Zeiss LSM 510 Meta) and percentages of cells showing actin rearrangements were manually quantified (at least 100 cells per cover glass were counted manually).

Chemotaxis assay

Isolated T or B cells from WT or Myo9b^{-/-} mice were added to 5 µm-pore size Transwell Chambers (Costar; 5×10^5 /well) and allowed to migrate toward 100 nM recombinant mouse CCL21, CXL12, CCL19, or CXCL13 for 1 h at 37°C. Chemotaxis efficiency and relative input were enumerated by flow cytometry. In some experiments, Transwell filters were coated with 5×10^4 Vero or Caco-2 cells for 48 h before lysis in distilled water for 30 min. Filters were coated with Laminin (Sigma; 0.5 µg/50 µl in DPBS) for 30 min at 4°C, followed by air drying for 2 h, or with 30 µl collagen gels polymerized at 37°C prepared as follows:

low-density collagen (1.6 mg/ml) was prepared by mixing 750 µl bovine collagen I (PureCol; Nutacon) with bicarbonate-buffered MEM (50 µl 7.5% NaHCO₃ and 100 µl 10× MEM; Gibco); high-density collagen (4.6 mg/ml) was prepared as described above using highly concentrated rat collagen I (Becton Dickinson). In some experiments, T cells were pretreated with Y27632 (20 µM), LIMK inhibitor S3 (10 mg/ml), MLCK inh (20 µM), or Rhosin (G04: 0.1–30 µM) for 1 h at 37°C, with inhibitors present during chemotaxis assays.

Shear resistant adhesion and in vitro crawling speed

In vitro live cell imaging under flow conditions and coating with recombinant mouse ICAM-1 (mICAM-1) was as described (Steiner et al., 2010). Before the experiments mICAM-1 was overlaid with CCL21. Naive T cells from WT or Myo9b^{-/-} mice were labeled with CMAC and CMTMR, respectively, adjusted to 10^7 cells/ml each, mixed in a 1-to-1 ratio and perfused over mICAM at low shear stress (0.1 dyn/cm²) for 3 to 4 min. Then, shear was increased to physiological strength at 1.5 dyn/cm² and maintained for 10 to 15 min. The complete experiment was recorded under 10× objective magnification (EC Plan; NA 0.4) with time lapse image acquisition using a monochrome charge-coupled device camera (Axio-Cam MRm Rev; Carl Zeiss) at 1 frame each 6 s. For evaluation of shear resistant sustained adhesion, we counted T cells/FOV at 20 to 30 s (accumulated T cells) and at 10 min (sustained adherent T cells) after onset of physiological flow and expressed numbers in percent of accumulated T cells (=100%). For crawling speed under physiological flow, time-lapse videos were analyzed using the Manual Tracking Plugin interfaced with ImageJ software (National Institutes of Health). Fluorescent live-cell images were acquired with an LCI Plan Neofluar 63×/NA 1.3 glycerol immersion objective and appropriate filters for CMTMR and CMAC.

Collagen motility assays

The assay was performed as previously described (Stolp et al., 2012). In brief, 3×10^6 splenocytes were stimulated o.n. with IL-2 (50 U/ml) and ConA (2 µg/ml), followed by WT and Myo9b^{-/-} T cell isolation (EasySep Mouse T cell Negative Selection kit; STEMCE LL Technologies). WT or Myo9b^{-/-} T cells (3×10^5 in 50 µl 0.5% FCS-reduced media) were mixed with 100 µl low-density collagen matrix (1.6 mg/ml) and allowed to polymerize at 37°C within self-constructed migration chambers. Gels were spiked with CCL21 100 nM (PeproTech) and sealed with melted dental wax. Micrographs were acquired every 60 s for 120 min at 37°C using a 10× objective (EC Plan; NA 0.4) with bright field on an inverse light microscope (10× objective, Axiovert 200M; Zeiss) coupled to an electron microscopic charge-coupled device camera (Roper Scientific). Migrating cells were tracked manually using the Fiji manual tracking plugin and analyzed with the chemotaxis tool plugin. We used 5 µm/min as threshold for arrest coefficient analysis.

Under agarose assay

Under agarose assays were essentially performed as described (Renkawitz et al., 2009). In brief, WT or Myo9b^{-/-} T cell blasts were injected between a glass coverslip and an agarose layer. Migrating cells were tracked manually using the Fiji manual tracking plugin and analyzed with the chemotaxis tool plugin.

Homing and 3D immunofluorescence

CFSE- and CMTMR-labeled WT and Myo9b^{-/-} T cells (10⁷/mouse) were coinjected i.v. into sex-matched 5- to 10-wk-old C57BL/6 recipient mice. At 2 h after adoptive transfer, blood was collected from the submandibular plexus, mice were killed using CO₂, and perfused with 5 ml cold PBS. PLN, MLN, and spleens were homogenized using a 70- μ m cell strainer. Cell suspension was analyzed using a FACS Calibur (BD) and FlowJo software (Tree Star). For three-dimensional immunofluorescence (3-DIF; Boscacci et al., 2010), 3 \times 10⁶ CMAC- and CMTMR-labeled WT and Myo9b^{-/-} purified T cells were coinjected i.v. into sex-matched 5- to 10-wk-old C57BL/6 recipient mice. 20 min after adoptive transfer, 100 μ g Mel-14 mAb (anti-L-selectin) and 5 μ g Alexa Fluor 633-conjugated MECA-79 mAb (anti-PNAd) were injected i.v.; 20 min later, mice were killed using CO₂, perfused with 5 ml cold PBS, and fixed in 10 ml cold 1% PFA/PBS. PLNs were collected and manually cleaned from surrounding fat tissue under a stereomicroscope. After o/n fixation in PBS/1% PFA, PLNs were embedded into 2% (wt/vol) agarose low gelling point (Sigma), dehydrated in methanol for 24 h, and cleared for at least 2 d in benzyl alcohol/benzyl benzoate (1:2 ratio). Blocks of agarose-embedded PLNs were imaged using a 2PM setup (TrimScope; LaVision Biotec). The absolute number of lymphocytes labeled with each dye was counted using Volocity software (PerkinElmer). Visual analysis of individual z-sections was used to determine the position of individual cells relative to the HEV network.

Extrapolating T cell tracks in lymph nodes and skin for simulation

To extrapolate short 2PM T cell tracks from the LN to “12 h” in silico tracks, we drew a random sample of their step sizes, turning angles, and plane angles, i.e., the angle between the planes of two consecutive turns. To account for autocorrelation, we calculated the means of the squared differences between consecutive step sizes and turning angles, neglecting the small autocorrelation in the plane angles. We then randomly exchanged steps if both these means of the synthetic tracks came closer to the means of the 2PM tracks. We stopped once both simulated means were smaller than the measured means. To simulate contact formation, we normally distributed 100 of these tracks with a standard deviation of 150 μ m, such that half of the tracks stayed for 11 h within the spherical T cell zone of 1-mm diameter. We then uniformly distributed 50 or 10⁴ static DCs within the T cell zone and assumed T cells closer than 15 μ m to form stable contacts. We repeated these simulations 50 times in each configuration to get stable distributions of the numbers of T cells in contact. Analogously, we extrapolated tracks from the skin to 24 h tracks in two dimensions by sampling and reshuffling step sizes and turning angles in the xy plane. The simulations were performed using Python and open source libraries for scientific computing (McKinney, 2010; Pedregosa et al., 2012; Waskom et al., 2014).

DC culture and peptide pulsing

Bone marrow cell suspensions from GFP-expressing mice were obtained by centrifugation (4,000 rpm; 4 min) of femurs and tibiae and incubated in 20-ml cultures containing 18 ml CM-R and 2 ml SP-20 supernatant containing Flt3L for 6 to 9 d. Cells

were stimulated with LPS (1 μ g/ml; Sigma-Aldrich) for 24 h and pulsed with indicated concentrations of OVA₂₅₇₋₂₆₄ peptide (SII NFEKEL; ECM Microtechnologies) for 45 min at 37°C.

2PM of popliteal LN

CMAC- or CMTMR-labeled WT or Myo9b^{-/-} polyclonal or OT-I CD8⁺ T cells (3 \times 10⁶) were adoptively transferred into C57BL/6 recipient mice. In some experiments, GFP⁺ DCs (2 \times 10⁶/mouse) were pulsed with 100 or 1000 nM OVA₂₅₇₋₂₆₄ peptide and s.c. injected into hind footpad of 5- to 10-wk-old sex-matched C57BL/6 mice 18 h before adoptive transfer. Immediately after injection, 2PM imaging (TrimScope) was performed with an Olympus BX50WI fluorescence microscope and a 20 \times objective (NA 0.95). For four-dimensional analysis of cell migration, 10–16 z-stacks (spacing 4 μ m) of 200- to 300- μ m² xy-sections were acquired every 6 to 20 s for 10 to 30 min. Imaging was performed in the T cell area identified by the presence of HEVs labeled using Alexa Fluor 633-conjugated MECA-79. Sequences of image stacks were transformed into volume-rendered four-dimensional videos using Volocity software (PerkinElmer), which was also used for semiautomated tracking of cell motility in three dimensions. The mean track velocity and turning angles (defined as the angle between the two velocity vectors before and after a measurement time point) were calculated from the x, y, and z coordinates of cell centroids (Mempel et al., 2004). The cutoff for arrest coefficient calculation was set to 4 μ m/min. To calculate two-dimensional “circularity,” LN Videos of four-dimensional volume-rendered datasets were generated using Volocity software and converted to image sequences with QuickTime Pro. Individual cell tracks of the image sequence were compared with their original four-dimensional-rendered image sequence to identify all time frames when cells were with the entire circumference inside the imaging volume, with time points where cells were only partially in the imaging volume being manually discarded using Adobe Photoshop. The shape factor of filtered image sequences was reanalyzed using Volocity software to yield circularity. To calculate three-dimensional “sphericity,” the shape factor of volume-rendered four-dimensional image sequences from skin videos was measured using Volocity software without any modification, because single cells remained present in the epidermis throughout the duration of the recording.

In vivo proliferation and flow cytometry for activation markers

DsRed⁺ WT and GFP⁺ OT-I Myo9b^{-/-} CD8⁺ T cells were labeled with e670 (5 μ M, 20 min) and analyzed for cell division and activation markers expression 24, 48, or 72 h after transfer into mice with pMHC-bearing DCs as described for 2PM experiments. Cell surface stainings were performed with the appropriate combinations of saturating concentrations of the following conjugated mAbs obtained from BioLegend: CD25 (3C7), CD69 (H1.2F3), CD103 (2E7), CXCR3 (CXCR3-173), CD127 (A019D5), KLRG1 (14C2A07), and CD8 (53-6.7). Flow cytometry was performed on a LSRII (Becton Dickinson) and FlowJo software (Tree Star) was used for analysis.

Viral infections

Ovalbumin-expressing rLCMV-OVA was generated according to established procedures (Emonet et al., 2009; Flatz et al., 2010).

WT or Myo9b^{-/-} CD8⁺ T cells (10⁴/mouse) were injected i.v. into different sex-matched 5- to 10-wk-old Ubi-GFP recipient mice. 24 h later, mice were i.p. infected with 10⁵ plaque-forming units (pfu) of LCMV-OVA. Mice were bled or killed at indicated days after infection for flow cytometry analysis. For HSV-1_{TOM}-OVA infections, GFP⁺ OT-I WT or Myo9b^{-/-} CD8⁺ T_{CM} (5 × 10⁵/mouse) isolated from spleens and LNs of LCMV-OVA-immunized mice at day 30 after infection were adoptively transferred into recipient mice. 1 d later, intraepithelial infection was performed on the shaved flank of anesthetized mice by tattooing a 10-μl drop-let containing 5 × 10⁵ pfu HSV-1_{TOM}-OVA encoding tandem dimer tomato and ovalbumin onto the skin using a sterile disposable 9-needle bar mounted on a rotary tattoo device as described (Ariotti et al., 2015). Vero cells, seeded in 6-well plates at a density of 4 × 10⁵ cells per well such that monolayers were confluent the following day, were infected with serial dilutions of homogenized skin biopsies (10-mm diameter; MagNA Lyser, Roche) for 45 min. After incubation in medium containing 0.5% methylcellulose for 72 h, plaques were identified by 0.1% crystal violet staining and counted. To assess T_{RM} function, 3 × 10⁵ dsRed⁺ WT or GFP⁺ Myo9b^{-/-} OT-I T cells were injected i.v. into sex-matched Prf1^{-/-} recipients. 1 d later, recipient mice were infected i.p. with 10⁵ pfu LCMV-OVA. On day 3 after infection, mice were anesthetized with ketamine/xylazine. One flank was shaved and residual hair removed with depilating cream before OVA₂₅₇₋₂₆₃ peptide (2.5 ng in 10 μl PBS/10% DMSO) was tattooed onto the shaved flank. During day 29 and 32 after infection, mice were treated daily with an i.p. injection of FTY720 (1 mg/kg in 0.9% NaCl; Sigma) to prevent recruitment of circulating cells to the skin during rechallenge. On day 30, HSV-1_{TOM}-OVA was tattooed into the skin of both flanks and viral titers determined as above. As controls, we infected untreated Prf1^{-/-} mice that had not received OT-I T cells to determine “no cells” viral titers.

Quantification of skin sections by immunohistology

Formalin-fixed paraffin-embedded consecutive sections (4 μm) were dewaxed and dehydrated by a graded decrease alcohol series and stained for histology or immunohistochemical characterization (IHC). For histological analysis in bright-field microscopy, slides were stained using standard protocols for H&E (using Mayer's H&E; BioOptica) and Sirius red staining (Direct Red 80, Sigma) for collagen fibers. For IHC, slides were immunostained for anti-GFP mAb (Thermo Fisher Scientific) and anti-RFP mAb (Rockland) according to the manufacturers' instructions. Control experiments showed that on day 8 after infection, no tdTomato-expressing HSV-1_{TOM}-OVA-infected cells were detectable in skin. After antigen unmasking with citrate buffer, pH 6.0, endogenous peroxidase activity was inhibited by incubating slides with 3% peroxidase water for 20 min at RT. Both mAbs were used at dilution of 1:200 and developed with EXPOSE rabbit-specific HRP/DAB detection IHC kit (ab80437). After immunostaining, DAB substrate chromogen was applied to sections for 5 min at RT and counterstained with Mayer's Hematoxylin, dehydrated, and mounted with Eukitt (BioOptica). Proper external positive and negative controls were run simultaneously. Slides were acquired with Aperio AT2 digital scanner at magnification of 200× (Leica Biosystems). Cells in epidermis and papillary dermis were counted manually.

2PM of skin

For skin intravital microscopy (IVM), the right flank of anesthetized mice was shaved and depilated using Veet (Reckitt Benckiser). Parallel incisions were made 15 mm apart in the skin flank before separating from the underlying peritoneum. A stable imaging platform was established by inserting an 18-mm stainless steel disk under the dermis. The underside of the dermis was glued to the steel disk using Vetbond tissue adhesive (3M). Images were acquired and analyzed as described above. For four-dimensional analysis of cell migration, 13–25 z-stacks (spacing 2.5 μm) of 250–450 μm² xy sections were acquired every 60 s for 1 to 2 h. Imaging was performed in the epidermis and in the dermis was identified by the presence of dermal collagen fibers identified by second harmonic green (SHG) signal. We also used SHG signal as anatomical reference channel for real-time offset correction to minimize tissue shift (Vladymyrov et al., 2016). In this system, SHG signal shifts between frames are detected through fast computational analysis for feedback to an automated stage that performs a corrective motion before the next stack is acquired. In some experiments, OVA₂₅₇₋₂₆₄ peptide (2.5 ng of peptide in PBS/10% DMSO) was tattooed in the flank of anesthetized mice before 2PM surgical preparation. Images were acquired from 1 to 8 h after OVA₂₅₇₋₂₆₄ delivery. Membrane protrusion analysis was performed on epidermal 2PM videos, using the ADAPT plugin for ImageJ (Barry et al., 2015). The mean protrusion speed per cell was calculated for a membrane protrusion size range of 0.2–5 μm².

Scanning electron microscopy

ECM-coated filters were produced as described in chemotaxis assays. 5 × 10⁴ Vero or CaCo-2 cells were seeded on top of 5 μm pore Transwell filters and incubated for 2 d at 37°C. Filters were fixed with 4% PFA (Merck) and 0.1% glutaraldehyde (Merck) in PBS for 1 h at room temperature. Samples were dehydrated through an ascending ethanol series and dried by evaporation of hexamethyldisilazane (Merck) as described previously (Stoffel and Friess, 2002). Samples were mounted on metal stubs with conductive adhesive pads (Ted Pella) and sputter-coated with ~20 nm of gold with an SCD004 Sputter Coater (BalTec). Secondary electron micrographs were obtained with a field emission scanning electron microscope DSM 982 Gemini (Zeiss) at an accelerating voltage of 5 kV at a working distance of 6–8 mm.

Analysis of in vitro cytotoxicity

DsRed⁺ WT or GFP Myo9b^{-/-} cells OT-I T_{CM} cells were isolated from skin of HSV-1_{TOM}-OVA-infected mice on day 30 after infection using BD FACSaria cell sorter. 10⁴ sorted WT or Myo9b^{-/-} cells were mixed with 5 × 10⁴ purified unpulsed B cells labeled with 0.5 μM e670 or 5 × 10⁴ OVA₂₅₇₋₂₆₄-pulsed B cells labeled with 10 μM e670 (20 min, 37°C). After 24 h at 37°C, 5% CO₂, cell suspensions were analyzed for the ratio of e670^{high} to e670^{low} B cells using a FACS Calibur (Becton Dickinson).

Statistical analysis

Data were analyzed using Prism 6 (GraphPad) using Student's *t* test, ANOVA, and nonparametric tests as indicated in the Figure legends. P-values <0.05 were considered significant.

Online supplemental material

Fig. S1 depicts the comparable phenotype of naive WT and Myo9b^{-/-} T cells. Fig. S2 describes lymphocyte compartments of WT and Myo9b^{-/-} mice with decreased cellularity in the latter. Fig. S3 shows comparable in vitro activation of WT and Myo9b^{-/-} T cells. Fig. S4 depicts the localization of WT and Myo9b^{-/-} OT-I T cells on day 8 after infection with HSV-1_{TOM-OVA}, with fewer epidermal Myo9b^{-/-} T cells. Fig. S5 shows the low Transwell migration of Myo9b^{-/-} T cells across the ECM layer of lysed epithelial cell lines. Videos 1 and 2 show largely comparable motility of naive WT and Myo9b^{-/-} T cells in lymphoid tissue (Video 2 is high temporal resolution mode). Video 3 depicts comparable interactions of WT and Myo9b^{-/-} OT-I T cells with peptide-loaded DCs. Videos 4 and 5 show WT and Myo9b^{-/-} OT-I T cells in epidermis. Video 6 shows WT and Myo9b^{-/-} OT-I T cells in dermis. Video 7 depicts migration of a dermal Myo9b^{-/-} OT-I T cell close to the epidermal layer.

Acknowledgments

We thank Ton Schumacher and colleagues (The Netherlands Cancer Research Center, Amsterdam, Netherlands) for helpful advice on the HSV-1_{TOM-OVA} skin infection model.

This work was funded by Swiss National Foundation (SNF) project grant 31003A_135649 (to J.V. Stein), interdisciplinary SNF grant CR23I3_156234 (to A. Ariga and J.V. Stein), Swiss Cancer League grant KFS-3524-08-2014 (to J.V. Stein), and a Bangerter-Rhyner fellowship (to F. Moalli). This work benefitted from data assembled by the ImmGen consortium and from optical setups of the Microscopy Imaging Center of the University of Bern. P. Germann and J. Sharpe acknowledge support of the Spanish Ministry of Economy and Competitiveness, Centro de Excelencia Severo Ochoa 2013–2017, and support of the CERCA Program/Generalitat de Catalunya.

The authors declare no competing financial interests.

Author contributions: F. Moalli, X. Ficht, B. Stolp, I. de Vries, A. Focchi, M. Kreutzfeldt, R. Lyck, and A. Diz-Muñoz performed experiments or prepared important reagents; J. Balmer performed experiments; P. Germann performed computational simulations under supervision of J. Sharpe; D. Merkler, A. Ariga, M.H. Stoffel, M. Bähler, M. Iannaccone, M. Sixt, A. Diz-Muñoz, and J.V. Stein supervised experiments and analysis. M. Vladymyrov provided software. F. Moalli and J.V. Stein wrote the manuscript with input from all coauthors.

Submitted: 30 May 2017

Revised: 28 December 2017

Accepted: 11 May 2018

References

- Alonso, J.L., and W.H. Goldmann. 2003. Feeling the forces: atomic force microscopy in cell biology. *Life Sci.* 72:2553–2560. [https://doi.org/10.1016/S0024-3205\(03\)00165-6](https://doi.org/10.1016/S0024-3205(03)00165-6)
- Ariotti, S., J.B. Beltman, G. Chodaczek, M.E. Hoekstra, A.E. van Beek, R. Gomez-Eerland, L. Ritsma, J. van Rheenen, A.F.M. Marée, T. Zal, et al. 2012. Tissue-resident memory CD8⁺ T cells continuously patrol skin epithelia to quickly recognize local antigen. *Proc. Natl. Acad. Sci. USA.* 109:19739–19744. <https://doi.org/10.1073/pnas.1208927109>
- Ariotti, S., M.A. Hogenbirk, F.E. Dijkgraaf, L.L. Visser, M.E. Hoekstra, J.Y. Song, H. Jacobs, J.B. Haanen, and T.N. Schumacher. 2014. Skin-resident memory CD8⁺ T cells trigger a state of tissue-wide pathogen alert. *Science.* 346:101–105. <https://doi.org/10.1126/science.1254803>
- Ariotti, S., J.B. Beltman, R. Borsje, M.E. Hoekstra, W.P. Halford, J.B.A.G. Haanen, R.J. de Boer, and T.N.M. Schumacher. 2015. Subtle CXCR3-Dependent Chemotaxis of CTLs within Infected Tissue Allows Efficient Target Localization. *J. Immunol.* 195:5285–5295. <https://doi.org/10.4049/jimmunol.1500853>
- Bajénoff, M., J.G. Egen, L.Y. Koo, J.P. Laugier, F. Brau, N. Glaichenhaus, and R.N. Germain. 2006. Stromal cell networks regulate lymphocyte entry, migration, and territoriality in lymph nodes. *Immunity.* 25:989–1001. <https://doi.org/10.1016/j.immuni.2006.10.011>
- Barry, D.J., C.H. Durkin, J.V. Abella, and M. Way. 2015. Open source software for quantification of cell migration, protrusions, and fluorescence intensities. *J. Cell Biol.* 209:163–180. <https://doi.org/10.1083/jcb.201501081>
- Bergert, M., A. Erzberger, R.A. Desai, I.M. Aspalter, A.C. Oates, G. Charras, G. Salbreux, and E.K. Paluch. 2015. Force transmission during adhesion-independent migration. *Nat. Cell Biol.* 17:524–529. <https://doi.org/10.1038/ncb3134>
- Boscacci, R.T., F. Pfeiffer, K. Gollmer, A.I.C. Sevilla, A.M. Martin, S.F. Soriano, D. Natale, S. Henrickson, U.H. von Andrian, Y. Fukui, et al. 2010. Comprehensive analysis of lymph node stroma-expressed Ig superfamily members reveals redundant and nonredundant roles for ICAM-1, ICAM-2, and VCAM-1 in lymphocyte homing. *Blood.* 116:915–925. <https://doi.org/10.1182/blood-2009-11-254334>
- Breitkreutz, D., N. Mirancea, and R. Nischt. 2009. Basement membranes in skin: unique matrix structures with diverse functions? *Histochem. Cell Biol.* 132:1–10. <https://doi.org/10.1007/s00418-009-0586-0>
- Bufl, N., M. Saitakis, S. Dogniaux, O. Buschinger, A. Bohineust, A. Richert, M. Maurin, C. Hivroz, and A. Asnacios. 2015. Human Primary Immune Cells Exhibit Distinct Mechanical Properties that Are Modified by Inflammation. *Biophys. J.* 108:2181–2190. <https://doi.org/10.1016/j.bpj.2015.03.047>
- Cahalan, M.D., and I. Parker. 2006. Imaging the choreography of lymphocyte trafficking and the immune response. *Curr. Opin. Immunol.* 18:476–482. <https://doi.org/10.1016/j.coi.2006.05.013>
- Cai, Y., O. Rossier, N.C. Gauthier, N. Biais, M.-A. Fardin, X. Zhang, L.W. Miller, B. Ladoux, V.W. Cornish, and M.P. Sheetz. 2010. Cytoskeletal coherence requires myosin-IIA contractility. *J. Cell Sci.* 123:413–423. <https://doi.org/10.1242/jcs.058297>
- Cauley, L.S., and L. Lefrançois. 2013. Guarding the perimeter: protection of the mucosa by tissue-resident memory T cells. *Mucosal Immunol.* 6:14–23. <https://doi.org/10.1038/mi.2012.96>
- Charras, G., and E. Sahai. 2014. Physical influences of the extracellular environment on cell migration. *Nat. Rev. Mol. Cell Biol.* 15:813–824. <https://doi.org/10.1038/nrm3897>
- Comrie, W.A., A. Babich, and J.K. Burkhardt. 2015. F-actin flow drives affinity maturation and spatial organization of LFA-1 at the immunological synapse. *J. Cell Biol.* 208:475–491. <https://doi.org/10.1083/jcb.201406121>
- Davies, B., J.E. Prier, C.M. Jones, T. Gebhardt, F.R. Carbone, and L.K. Mackay. 2017. Cutting Edge: Tissue-Resident Memory T Cells Generated by Multiple Immunizations or Localized Deposition Provide Enhanced Immunity. *J. Immunol.* 198:2233–2237. <https://doi.org/10.4049/jimmunol.1601367>
- Dejana, E., and F. Orsenigo. 2013. Endothelial adherens junctions at a glance. *J. Cell Sci.* 126:2545–2549. <https://doi.org/10.1242/jcs.124529>
- Diz-Muñoz, A., D.A. Fletcher, and O.D. Weiner. 2013. Use the force: membrane tension as an organizer of cell shape and motility. *Trends Cell Biol.* 23:47–53. <https://doi.org/10.1016/j.tcb.2012.09.006>
- Dustin, M.L. 2004. Stop and go traffic to tune T cell responses. *Immunity.* 21:305–314. <https://doi.org/10.1016/j.immuni.2004.08.016>
- Dustin, M.L., and D. Depoil. 2011. New insights into the T cell synapse from single molecule techniques. *Nat. Rev. Immunol.* 11:672–684. <https://doi.org/10.1038/nri3066>
- Emonet, S.F., L. Garidou, D.B. McGavern, and J.C. de la Torre. 2009. Generation of recombinant lymphocytic choriomeningitis viruses with trisegmented genomes stably expressing two additional genes of interest. *Proc. Natl. Acad. Sci. USA.* 106:3473–3478. <https://doi.org/10.1073/pnas.0900088106>
- Faroudi, M., M. Hons, A. Zachacz, C. Dumont, R. Lyck, J.V. Stein, and V.L.J. Tybulewicz. 2010. Critical roles for Rac GTPases in T-cell migration to and within lymph nodes. *Blood.* 116:5536–5547. <https://doi.org/10.1182/blood-2010-08-299438>
- Flatz, L., A.N. Hegazy, A. Berghaler, A. Verschoor, C. Claus, M. Fernandez, L. Gattinoni, S. Johnson, F. Kreppel, S. Kochanek, et al. 2010. Development

- of replication-defective lymphocytic choriomeningitis virus vectors for the induction of potent CD8⁺ T cell immunity. *Nat. Med.* 16:339–345. <https://doi.org/10.1038/nm.2104>
- Friedl, P., and B. Weigelin. 2008. Interstitial leukocyte migration and immune function. *Nat. Immunol.* 9:960–969. <https://doi.org/10.1038/ni.f.212>
- Fritz-Laylin, L.K., S.J. Lord, and R.D. Mullins. 2017. WASP and SCAR are evolutionarily conserved in actin-filled pseudopod-based motility. *J. Cell Biol.* 216:1673–1688. <https://doi.org/10.1083/jcb.201701074>
- Froehlich, J., M. Versapuech, L. Megrelis, Q. Largeteau, S. Meunier, C. Tanchot, G. Bismuth, J. Delon, and M. Mangeney. 2016. FAM65B controls the proliferation of transformed and primary T cells. *Oncotarget.* 7:63215–63225. <https://doi.org/10.18632/oncotarget.11438>
- Furuse, M. 2009. Knockout animals and natural mutations as experimental and diagnostic tool for studying tight junction functions in vivo. *Biochim. Biophys. Acta.* 1788:813–819. <https://doi.org/10.1016/j.bbame.2008.07.017>
- Gauthier, N.C., T.A. Masters, and M.P. Sheetz. 2012. Mechanical feedback between membrane tension and dynamics. *Trends Cell Biol.* 22:527–535. <https://doi.org/10.1016/j.tcb.2012.07.005>
- Gebhardt, T., and L.K. Mackay. 2012. Local immunity by tissue-resident CD8⁺ memory T cells. *Front. Immunol.* 3:340. <https://doi.org/10.3389/fimmu.2012.00340>
- Gebhardt, T., P.G. Whitney, A. Zaid, L.K. Mackay, A.G. Brooks, W.R. Heath, F.R. Carbone, and S.N. Mueller. 2011. Different patterns of peripheral migration by memory CD4⁺ and CD8⁺ T cells. *Nature.* 477:216–219. <https://doi.org/10.1038/nature10339>
- Gérard, A., G. Patiño-López, P. Beemiller, R. Nambiar, K. Ben-Aissa, Y. Liu, F.J. Totah, M.J. Tyska, S. Shaw, and M.F. Krummel. 2014. Detection of rare antigen-presenting cells through T cell-intrinsic meandering motility, mediated by Myo1g. *Cell.* 158:492–505. <https://doi.org/10.1016/j.cell.2014.05.044>
- Gerlach, C., E.A. Moseman, S.M. Loughhead, D. Alvarez, A.J. Zwijnenburg, L. Waanders, R. Garg, J.C. de la Torre, and U.H. von Andrian. 2016. The Chemokine Receptor CX3CR1 Defines Three Antigen-Experienced CD8⁺ T Cell Subsets with Distinct Roles in Immune Surveillance and Homeostasis. *Immunity.* 45:1270–1284. <https://doi.org/10.1016/j.immuni.2016.01.018>
- Guillou, L., A. Babataheri, M. Saitakis, A. Bohineust, S. Dogniaux, C. Hivroz, A.I. Barakat, and J. Husson. 2016. T-lymphocyte passive deformation is controlled by unfolding of membrane surface reservoirs. *Mol. Biol. Cell.* 27:3574–3582. <https://doi.org/10.1091/mbc.e16-06-0414>
- Hanley, P.J., Y. Xu, M. Kronlage, K. Grobe, P. Schön, J. Song, L. Sorokin, A. Schwab, and M. Bähler. 2010. Motorized RhoGAP myosin IXb (Myo9b) controls cell shape and motility. *Proc. Natl. Acad. Sci. USA.* 107:12145–12150. <https://doi.org/10.1073/pnas.0911986107>
- Hashimoto-Tane, A., M. Sakuma, H. Ike, T. Yokosuka, Y. Kimura, O. Ohara, and T. Saito. 2016. Micro-adhesion rings surrounding TCR microclusters are essential for T cell activation. *J. Exp. Med.* 213:1609–1625. <https://doi.org/10.1084/jem.20151088>
- Heng, T.S.P., and M.W. Painter. Immunological Genome Project Consortium. 2008. The Immunological Genome Project: networks of gene expression in immune cells. *Nat. Immunol.* 9:1091–1094. <https://doi.org/10.1038/ni1008-1091>
- Hogquist, K.A., S.C. Jameson, W.R. Heath, J.L. Howard, M.J. Bevan, and F.R. Carbone. 1994. T cell receptor antagonist peptides induce positive selection. *Cell.* 76:17–27. [https://doi.org/10.1016/0092-8674\(94\)90169-4](https://doi.org/10.1016/0092-8674(94)90169-4)
- Huang, A.Y.C., H. Qi, and R.N. Germain. 2004. Illuminating the landscape of in vivo immunity: insights from dynamic in situ imaging of secondary lymphoid tissues. *Immunity.* 21:331–339. <https://doi.org/10.1016/j.immuni.2004.08.001>
- Huber, A.R., and S.J. Weiss. 1989. Disruption of the subendothelial basement membrane during neutrophil diapedesis in an in vitro construct of a blood vessel wall. *J. Clin. Invest.* 83:1122–1136. <https://doi.org/10.1172/JCI113992>
- Hui, K.L., and A. Upadhyaya. 2017. Dynamic microtubules regulate cellular contractility during T-cell activation. *Proc. Natl. Acad. Sci. USA.* 114:E4175–E4183. <https://doi.org/10.1073/pnas.1614291114>
- Iijima, N., and A. Iwasaki. 2014. T cell memory. A local macrophage chemokine network sustains protective tissue-resident memory CD4⁺ T cells. *Science.* 346:93–98. <https://doi.org/10.1126/science.1257530>
- Iijima, N., and A. Iwasaki. 2015. Tissue instruction for migration and retention of TRM cells. *Trends Immunol.* 36:556–564. <https://doi.org/10.1016/j.it.2015.07.002>
- Jacobelli, J., R.S. Friedman, M.A. Conti, A.-M. Lennon-Dumenil, M. Piel, C.M. Sorensen, R.S. Adelstein, and M.F. Krummel. 2010. Confinement-optimized three-dimensional T cell amoeboid motility is modulated via myosin IIA-regulated adhesions. *Nat. Immunol.* 11:953–961. <https://doi.org/10.1038/ni.1936>
- Jiang, X., R.A. Clark, L. Liu, A.J. Wagers, R.C. Fuhlbrigge, and T.S. Kupper. 2012. Skin infection generates non-migratory memory CD8⁺ T(RM) cells providing global skin immunity. *Nature.* 483:227–231. <https://doi.org/10.1038/nature10851>
- Johnson, J.L., J. Monfregola, G. Napolitano, W.B. Kiess, and S.D. Catz. 2012. Vesicular trafficking through cortical actin during exocytosis is regulated by the Rab27a effector JFC1/Slp1 and the RhoA-GTPase-activating protein Gem-interacting protein. *Mol. Biol. Cell.* 23:1902–1916. <https://doi.org/10.1091/mbc.e11-12-1001>
- Kadoki, M., A. Patil, C.C. Thaiss, D.J. Brooks, S. Pandey, D. Deep, D. Alvarez, U.H. von Andrian, A.J. Wagers, K. Nakai, et al. 2017. Organism-Level Analysis of Vaccination Reveals Networks of Protection across Tissues. *Cell.* 171:398–413.e21. <https://doi.org/10.1016/j.cell.2017.08.024>
- Kalluri, R. 2003. Basement membranes: structure, assembly and role in tumour angiogenesis. *Nat. Rev. Cancer.* 3:422–433. <https://doi.org/10.1038/nrc1094>
- Katakai, T., K. Habiro, and T. Kinashi. 2013. Dendritic cells regulate high-speed interstitial T cell migration in the lymph node via LFA-1/ICAM-1. *J. Immunol.* 191:1188–1199. <https://doi.org/10.4049/jimmunol.1300739>
- Kearney, E.R., K.A. Pape, D.Y. Loh, and M.K. Jenkins. 1994. Visualization of peptide-specific T cell immunity and peripheral tolerance induction in vivo. *Immunity.* 1:327–339. [https://doi.org/10.1016/1074-7613\(94\)90084-1](https://doi.org/10.1016/1074-7613(94)90084-1)
- Khan, T.N., J.L. Mooster, A.M. Kilgore, J.F. Osborn, and J.C. Nolz. 2016. Local antigen in nonlymphoid tissue promotes resident memory CD8⁺ T cell formation during viral infection. *J. Exp. Med.* 213:951–966. <https://doi.org/10.1084/jem.20151855>
- Kirby, A.C., M.C. Coles, and P.M. Kaye. 2009. Alveolar macrophages transport pathogens to lung draining lymph nodes. *J. Immunol.* 183:1983–1989. <https://doi.org/10.4049/jimmunol.0901089>
- Krieg, M., Y. Arboleda-Estudillo, P.H. Puech, J. Käfer, F. Graner, D.J. Müller, and C.P. Heisenberg. 2008. Tensile forces govern germ-layer organization in zebrafish. *Nat. Cell Biol.* 10:429–436. <https://doi.org/10.1038/ncb1705>
- Krummel, M.F., and I. Macara. 2006. Maintenance and modulation of T cell polarity. *Nat. Immunol.* 7:1143–1149. <https://doi.org/10.1038/ni1404>
- Krummel, M.F., R.S. Friedman, and J. Jacobelli. 2014. Modes and mechanisms of T cell motility: roles for confinement and Myosin-IIA. *Curr. Opin. Cell Biol.* 30:9–16. <https://doi.org/10.1016/j.ccb.2014.05.003>
- Lämmermann, T., and M. Sixt. 2009. Mechanical modes of ‘amoeboid’ cell migration. *Curr. Opin. Cell Biol.* 21:636–644. <https://doi.org/10.1016/j.ccb.2009.05.003>
- Le Floch, A., and M. Huse. 2015. Molecular mechanisms and functional implications of polarized actin remodeling at the T cell immunological synapse. *Cell. Mol. Life Sci.* 72:537–556. <https://doi.org/10.1007/s00018-014-1760-7>
- Liu, Y.-J., M. Le Berre, F. Lautenschlaeger, P. Maiuri, A. Callan-Jones, M. Heuzé, T. Takaki, R. Voituriez, and M. Piel. 2015. Confinement and low adhesion induce fast amoeboid migration of slow mesenchymal cells. *Cell.* 160:659–672. <https://doi.org/10.1016/j.cell.2015.01.007>
- Mackay, L.K., and A. Kallies. 2017. Transcriptional Regulation of Tissue-Resident Lymphocytes. *Trends Immunol.* 38:94–103. <https://doi.org/10.1016/j.it.2016.11.004>
- Mackay, L.K., A.T. Stock, J.Z. Ma, C.M. Jones, S.J. Kent, S.N. Mueller, W.R. Heath, F.R. Carbone, and T. Gebhardt. 2012. Long-lived epithelial immunity by tissue-resident memory T (TRM) cells in the absence of persisting local antigen presentation. *Proc. Natl. Acad. Sci. USA.* 109:7037–7042. <https://doi.org/10.1073/pnas.1202288109>
- Mackay, L.K., A. Rahimpour, J.Z. Ma, N. Collins, A.T. Stock, M.-L. Hafon, J. Vega-Ramos, P. Lauzurica, S.N. Mueller, T. Stefanovic, et al. 2013. The developmental pathway for CD103⁺CD8⁺ tissue-resident memory T cells of skin. *Nat. Immunol.* 14:1294–1301. <https://doi.org/10.1038/ni.2744>
- McKinney, W. 2010. Data Structures for Statistical Computing in Python. Proceedings of the 9th Python in Science Conference. 51–56.
- Mempel, T.R., S.E. Henrickson, and U.H. Von Andrian. 2004. T-cell priming by dendritic cells in lymph nodes occurs in three distinct phases. *Nature.* 427:154–159. <https://doi.org/10.1038/nature02238>
- Mionnet, C., S.L. Sanos, I. Mondor, A. Jorquera, J.-P. Laugier, R.N. Germain, and M. Băjénoff. 2011. High endothelial venules as traffic control points maintaining lymphocyte population homeostasis in lymph nodes. *Blood.* 118:6115–6122. <https://doi.org/10.1182/blood-2011-07-367409>
- Morin, N.A., P.W. Oakes, Y.-M. Hyun, D. Lee, Y.E. Chin, M.R. King, T.A. Springer, M. Shimaoka, J.X. Tang, J.S. Reichner, and M. Kim. 2008. Nonmuscle myosin heavy chain IIA mediates integrin LFA-1 de-adhesion

- during T lymphocyte migration. *J. Exp. Med.* 205:195–205. <https://doi.org/10.1084/jem.20071543>
- Mueller, S.N., and L.K. Mackay. 2016. Tissue-resident memory T cells: local specialists in immune defence. *Nat. Rev. Immunol.* 16:79–89. <https://doi.org/10.1038/nri.2015.3>
- Mueller, S.N., T. Gebhardt, F.R. Carbone, and W.R. Heath. 2013. Memory T cell subsets, migration patterns, and tissue residence. *Annu. Rev. Immunol.* 31:137–161. <https://doi.org/10.1146/annurev-immunol-032712-095954>
- Murugesan, S., J. Hong, J. Yi, D. Li, J.R. Beach, L. Shao, J. Meinhardt, G. Madison, X. Wu, E. Betzig, and J.A. Hammer. 2016. Formin-generated actomyosin arcs propel T cell receptor microcluster movement at the immune synapse. *J. Cell Biol.* 215:383–399. <https://doi.org/10.1083/jcb.201603080>
- Niggli, V. 2003. Microtubule-disruption-induced and chemotactic-peptide-induced migration of human neutrophils: implications for differential sets of signalling pathways. *J. Cell Sci.* 116:813–822. <https://doi.org/10.1242/jcs.00306>
- Niggli, V. 2014. Insights into the mechanism for dictating polarity in migrating T-cells. *Int. Rev. Cell Mol. Biol.* 312:201–270. <https://doi.org/10.1016/B978-0-12-800178-3.00007-5>
- Nolz, J.C. 2015. Molecular mechanisms of CD8(+) T cell trafficking and localization. *Cell. Mol. Life Sci.* 72:2461–2473. <https://doi.org/10.1007/s00018-015-1835-0>
- Nourshargh, S., P.L. Hordijk, and M. Sixt. 2010. Breaching multiple barriers: leukocyte motility through venular walls and the interstitium. *Nat. Rev. Mol. Cell Biol.* 11:366–378. <https://doi.org/10.1038/nrm2889>
- Novkovic, M., L. Onder, J. Cupovic, J. Abe, D. Bomze, V. Cremasco, E. Scandella, J.V. Stein, G. Bocharov, S.J. Turley, and B. Ludewig. 2016. Topological Small-World Organization of the Fibroblastic Reticular Cell Network Determines Lymph Node Functionality. *PLoS Biol.* 14:e1002515. <https://doi.org/10.1371/journal.pbio.1002515>
- Osborn, J.F., J.L. Mooster, S.J. Hobbs, M.W. Munks, C. Barry, J.T. Harty, A.B. Hill, and J.C. Nolz. 2017. Enzymatic synthesis of core 2 O-glycans governs the tissue-trafficking potential of memory CD8⁺ T cells. *Sci. Immunol.* 2:eaan6049. <https://doi.org/10.1126/sciimmunol.aan6049>
- Ozga, A.J., F. Moalli, J. Abe, J. Swoger, D. Sharpe, D. Zehn, M. Kreutzfeldt, D. Merkler, J. Ripoll, and J.V. Stein. 2016. pMHC affinity controls duration of CD8⁺ T cell-DC interactions and imprints timing of effector differentiation versus expansion. *J. Exp. Med.* 213:2811–2829. <https://doi.org/10.1084/jem.20160206>
- Paluch, E.K., I.M. Aspalter, and M. Sixt. 2016. Focal Adhesion-Independent Cell Migration. *Annu. Rev. Cell Dev. Biol.* 32:469–490. <https://doi.org/10.1146/annurev-cellbio-111315-125341>
- Pan, Y., T. Tian, C.O. Park, S.Y. Lofftus, S. Mei, X. Liu, C. Luo, J.T. O'Malley, A. Gehad, J.E. Teague, et al. 2017. Survival of tissue-resident memory T cells requires exogenous lipid uptake and metabolism. *Nature*. 543:252–256. <https://doi.org/10.1038/nature21379>
- Pedregosa, F., G. Varoquaux, A. Gramfort, V. Michel, B. Thirion, O. Grisel, M. Blondel, P. Prettenhofer, R. Weiss, V. Dubourg, et al. 2012. Scikit-learn: Machine Learning in Python. *J. Mach. Learn. Res.* 12:2825–2830.
- Pfeiffer, F., V. Kumar, S. Butz, D. Vestweber, B.A. Imhof, J.V. Stein, and B. Engelhardt. 2008. Distinct molecular composition of blood and lymphatic vascular endothelial cell junctions establishes specific functional barriers within the peripheral lymph node. *Eur. J. Immunol.* 38:2142–2155. <https://doi.org/10.1002/eji.200838140>
- Prakash, M.D., M.A. Munoz, R. Jain, P.L. Tong, A. Koskinen, M. Regner, O. Kleinfeld, B. Ho, M. Olson, S.J. Turner, et al. 2014. Granzyme B promotes cytotoxic lymphocyte transmigration via basement membrane remodeling. *Immunity*. 41:960–972. <https://doi.org/10.1016/j.immuni.2014.11.012>
- Renkawitz, J., and M. Sixt. 2010. Mechanisms of force generation and force transmission during interstitial leukocyte migration. *EMBO Rep.* 11:744–750. <https://doi.org/10.1038/embor.2010.147>
- Renkawitz, J., K. Schumann, M. Weber, T. Lämmermann, H. Pflücke, M. Piel, J. Polleux, J.P. Spatz, and M. Sixt. 2009. Adaptive force transmission in amoeboid cell migration. *Nat. Cell Biol.* 11:1438–1443. <https://doi.org/10.1038/ncb1992>
- Ridley, A.J. 2011. Life at the leading edge. *Cell*. 145:1012–1022. <https://doi.org/10.1016/j.cell.2011.06.010>
- Rosenbluth, M.J., W.A. Lam, and D.A. Fletcher. 2006. Force microscopy of nonadherent cells: a comparison of leukemia cell deformability. *Biophys. J.* 90:2994–3003. <https://doi.org/10.1529/biophysj.105.067496>
- Rougerie, P., and J. Delon. 2012. Rho GTPases: masters of T lymphocyte migration and activation. *Immunol. Lett.* 142:1–13. <https://doi.org/10.1016/j.imlet.2011.12.003>
- Rowe, R.G., and S.J. Weiss. 2008. Breaching the basement membrane: who, when and how? *Trends Cell Biol.* 18:560–574. <https://doi.org/10.1016/j.tcb.2008.08.007>
- Ruprecht, V., S. Wieser, A. Callan-Jones, M. Smutny, H. Morita, K. Sako, V. Barone, M. Ritsch-Marte, M. Sixt, R. Voituriez, and C.-P. Heisenberg. 2015. Cortical contractility triggers a stochastic switch to fast amoeboid cell motility. *Cell*. 160:673–685. <https://doi.org/10.1016/j.cell.2015.01.008>
- Sallusto, F., J. Geginat, and A. Lanzavecchia. 2004. Central memory and effector memory T cell subsets: function, generation, and maintenance. *Annu. Rev. Immunol.* 22:745–763. <https://doi.org/10.1146/annurev.immunol.22.012703.104702>
- Salmon, H., K. Franciszkiewicz, D. Damotte, M.-C. Dieu-Nosjean, P. Validire, A. Trautmann, F. Mami-Chouaib, and E. Donnadieu. 2012. Matrix architecture defines the preferential localization and migration of T cells into the stroma of human lung tumors. *J. Clin. Invest.* 122:899–910. <https://doi.org/10.1172/JCI45817>
- Schaefer, B.C., M.L. Schaefer, J.W. Kappler, P. Marrack, and R.M. Kedl. 2001. Observation of antigen-dependent CD8⁺ T-cell/ dendritic cell interactions in vivo. *Cell. Immunol.* 214:110–122. <https://doi.org/10.1006/cimm.2001.1895>
- Schenkel, J.M., and D. Masopust. 2014. Tissue-resident memory T cells. *Immunity*. 41:886–897. <https://doi.org/10.1016/j.immuni.2014.12.007>
- Schenkel, J.M., K.A. Fraser, L.K. Beura, K.E. Pauken, V. Vezys, and D. Masopust. 2014. Resident memory CD8 T cells trigger protective innate and adaptive immune responses. *Science*. 346:98–101. <https://doi.org/10.1126/science.1254536>
- Schwab, S.R., and J.G. Cyster. 2007. Finding a way out: lymphocyte egress from lymphoid organs. *Nat. Immunol.* 8:1295–1301. <https://doi.org/10.1038/nri1545>
- Shang, X., F. Marchioni, N. Sipes, C.R. Evelyn, M. Jerabek-Willemsen, S. Dühr, W. Seibel, M. Wortman, and Y. Zheng. 2012. Rational design of small molecule inhibitors targeting RhoA subfamily Rho GTPases. *Chem. Biol.* 19:699–710. <https://doi.org/10.1016/j.chembiol.2012.05.009>
- Shin, H., and A. Iwasaki. 2012. A vaccine strategy that protects against genital herpes by establishing local memory T cells. *Nature*. 491:463–467. <https://doi.org/10.1038/nature11522>
- Smith, A., M. Bracke, B. Leitinger, J.C. Porter, and N. Hogg. 2003. LFA-1-induced T cell migration on ICAM-1 involves regulation of MLCK-mediated attachment and ROCK-dependent detachment. *J. Cell Sci.* 116:3123–3133. <https://doi.org/10.1242/jcs.00606>
- Smith, C.J., S. Caldeira-Dantas, H. Turula, and C.M. Snyder. 2015. Murine CMV Infection Induces the Continuous Production of Mucosal Resident T Cells. *Cell Reports*. 13:1137–1148. <https://doi.org/10.1016/j.celrep.2015.09.076>
- Soriano, S.F., M. Hons, K. Schumann, V. Kumar, T.J. Dennier, R. Lyck, M. Sixt, and J.V. Stein. 2011. In vivo analysis of uropod function during physiological T cell trafficking. *J. Immunol.* 187:2356–2364. <https://doi.org/10.4049/jimmunol.1100935>
- Sorokin, L. 2010. The impact of the extracellular matrix on inflammation. *Nat. Rev. Immunol.* 10:712–723. <https://doi.org/10.1038/nri2852>
- Stary, G., A. Olive, A.F. Radovic-Moreno, D. Gondek, D. Alvarez, P.A. Basto, M. Perro, V.D. Vrbanc, A.M. Tager, J. Shi, et al. 2015. VACCINES. A mucosal vaccine against Chlamydia trachomatis generates two waves of protective memory T cells. *Science*. 348:aaa8205. <https://doi.org/10.1126/science.aaa8205>
- Steinbach, K., I. Vincenti, M. Kreutzfeldt, N. Page, A. Muschawekch, I. Wagner, I. Drexler, D. Pinschewer, T. Korn, and D. Merkler. 2016. Brain-resident memory T cells represent an autonomous cytotoxic barrier to viral infection. *J. Exp. Med.* 213:1571–1587. <https://doi.org/10.1084/jem.20151916>
- Steiner, O., C. Coisne, R. Cecchelli, R. Boscacci, U. Deutsch, B. Engelhardt, and R. Lyck. 2010. Differential roles for endothelial ICAM-1, ICAM-2, and VCAM-1 in shear-resistant T cell arrest, polarization, and directed crawling on blood-brain barrier endothelium. *J. Immunol.* 185:4846–4855. <https://doi.org/10.4049/jimmunol.0903732>
- Stoffel, M.H., and A.E. Friess. 2002. Demonstration and cytochemical analysis of anionic sites on ejaculated boar spermatozoa: a scanning electron microscopy study using cationised colloidal gold. *Histochem. Cell Biol.* 117:61–67. <https://doi.org/10.1007/s00418-001-0350-6>
- Stolp, B., A. Imle, F.M. Coelho, M. Hons, R. Gorina, R. Lyck, J.V. Stein, and O.T. Fackler. 2012. HIV-1 Nef interferes with T-lymphocyte circulation through confined environments in vivo. *Proc. Natl. Acad. Sci. USA*. 109:18541–18546. <https://doi.org/10.1073/pnas.1204322109>
- Sumen, C., T.R. Mempel, I.B. Mazo, and U.H. von Andrian. 2004. Intravital microscopy: visualizing immunity in context. *Immunity*. 21:315–329. <https://doi.org/10.1016/j.immuni.2004.08.006>

- Thauland, T.J., K.H. Hu, M.A. Bruce, and M.J. Butte. 2017. Cytoskeletal adaptivity regulates T cell receptor signaling. *Sci. Signal.* 10:eaah3737. <https://doi.org/10.1126/scisignal.aah3737>
- Thom, J.T., T.C. Weber, S.M. Walton, N. Torti, and A. Oxenius. 2015. The Salivary Gland Acts as a Sink for Tissue-Resident Memory CD8(+) T Cells, Facilitating Protection from Local Cytomegalovirus Infection. *Cell Reports.* 13:1125–1136. <https://doi.org/10.1016/j.celrep.2015.09.082>
- Tietz, S., and B. Engelhardt. 2015. Brain barriers: Crosstalk between complex tight junctions and adherens junctions. *J. Cell Biol.* 209:493–506. <https://doi.org/10.1083/jcb.201412147>
- Tscharke, D.C., N.P. Croft, P.C. Doherty, and N.L. La Gruta. 2015. Sizing up the key determinants of the CD8(+) T cell response. *Nat. Rev. Immunol.* 15:705–716. <https://doi.org/10.1038/nri3905>
- Tybulewicz, V.L.J., and R.B. Henderson. 2009. Rho family GTPases and their regulators in lymphocytes. *Nat. Rev. Immunol.* 9:630–644. <https://doi.org/10.1038/nri2606>
- van den Boom, F., H. Düsselmann, K. Uhlenbrock, M. Abouhamed, and M. Bähler. 2007. The Myosin IXb motor activity targets the myosin IXb RhoGAP domain as cargo to sites of actin polymerization. *Mol. Biol. Cell.* 18:1507–1518. <https://doi.org/10.1091/mbc.e06-08-0771>
- Vargas, P., P. Maiuri, M. Bretou, P.J. Sáez, P. Pierobon, M. Maurin, M. Chaudaud, D. Lankar, D. Obino, E. Terriac, et al. 2016. Innate control of actin nucleation determines two distinct migration behaviours in dendritic cells. *Nat. Cell Biol.* 18:43–53. <https://doi.org/10.1038/ncb3284>
- Vestweber, D. 2015. How leukocytes cross the vascular endothelium. *Nat. Rev. Immunol.* 15:692–704. <https://doi.org/10.1038/nri3908>
- Vladymyrov, M., J. Abe, F. Moalli, J.V. Stein, and A. Ariga. 2016. Real-time tissue offset correction system for intravital multiphoton microscopy. *J. Immunol. Methods.* 438:35–41. <https://doi.org/10.1016/j.jim.2016.08.004>
- von Andrian, U.H., and C.R. Mackay. 2000. T-cell function and migration. Two sides of the same coin. *N. Engl. J. Med.* 343:1020–1034. <https://doi.org/10.1056/NEJM200010053431407>
- Wang, S., M.-B. Voisin, K.Y. Larbi, J. Dangerfield, C. Scheiermann, M. Tran, P.H. Maxwell, L. Sorokin, and S. Nourshargh. 2006. Venular basement membranes contain specific matrix protein low expression regions that act as exit points for emigrating neutrophils. *J. Exp. Med.* 203:1519–1532. <https://doi.org/10.1084/jem.20051210>
- Waskom, M., K. Meyer, P. Hobson, Y. Halchenko, M. Koskinen, A. Miles, D. Wehner, O. Botvinnik, and T. Megies. cynddl, et al. 2014. seaborn: v0.5.0. Available at: <https://github.com/mwaskom/seaborn/tree/v0.5.0> (accessed November 14, 2014).
- Wolf, K., M. Te Lindert, M. Krause, S. Alexander, J. Te Riet, A.L. Willis, R.M. Hoffman, C.G. Figdor, S.J. Weiss, and P. Friedl. 2013. Physical limits of cell migration: control by ECM space and nuclear deformation and tuning by proteolysis and traction force. *J. Cell Biol.* 201:1069–1084. <https://doi.org/10.1083/jcb.201210152>
- Woolf, E., I. Grigorova, A. Sagiv, V. Grabovsky, S.W. Feigelson, Z. Shulman, T. Hartmann, M. Sixt, J.G. Cyster, and R. Alon. 2007. Lymph node chemokines promote sustained T lymphocyte motility without triggering stable integrin adhesiveness in the absence of shear forces. *Nat. Immunol.* 8:1076–1085. <https://doi.org/10.1038/ni1499>
- Xu, J., F. Wang, A. Van Keymeulen, M. Rentel, and H.R. Bourne. 2005. Neutrophil microtubules suppress polarity and enhance directional migration. *Proc. Natl. Acad. Sci. USA.* 102:6884–6889. <https://doi.org/10.1073/pnas.0502106102>
- Xu, Y., S. Pektor, S. Balkow, S.A. Hemkemeyer, Z. Liu, K. Grobe, P.J. Hanley, L. Shen, M. Bros, T. Schmidt, et al. 2014. Dendritic cell motility and T cell activation requires regulation of Rho-cofilin signaling by the Rho-GTPase activating protein myosin IXb. *J. Immunol.* 192:3559–3568. <https://doi.org/10.4049/jimmunol.1300695>
- Yousif, L.F., J. Di Russo, and L. Sorokin. 2013. Laminin isoforms in endothelial and perivascular basement membranes. *Cell Adhes. Migr.* 7:101–110. <https://doi.org/10.4161/cam.22680>
- Zhou, P., D.R. Shaffer, D.A. Alvarez Arias, Y. Nakazaki, W. Pos, A.J. Torres, V. Cremasco, S.K. Dougan, G.S. Cowley, K. Elpek, et al. 2014. In vivo discovery of immunotherapy targets in the tumour microenvironment. *Nature.* 506:52–57. <https://doi.org/10.1038/nature12988>